学位論文　（要約）

Control of Structures and Properties of Transition Metal Oxide Thin Films by Soft Chemical Processes

（ソフト化学的手法による遷移金属酸化物薄膜の構造・特性制御）

平成 29 年 12 月博士（理学）申請

東京大学大学院理学系研究科

化学専攻

小野塚　智也

Control of Structures and Properties of Transition Metal Oxide Thin Films by Soft Chemical Processes

by

Tomoya Onozuka

Department of Chemistry

Graduate School of Science

The University of Tokyo

December, 2017

Abstract

1. Introduction

Transition-metal oxides are rich sources of interesting phenomena such as superconductivity, multiferroicity, and metal–insulator transition. Traditionally, they have been synthesized using a sintering process, where a mixture of starting metal oxides is heated up to high (> 1000 °C) temperature. On the other hand much attention has been paid to soft chemical, or low-temperature processes for the synthesis of metal oxide samples in the past several decades. Among them, topotactic reactions, during which a large part of the crystal structure of the starting material is maintained, are rather kinetic process because they exploit higher mobility of particular elements over others in a single material, and thus they are powerful methods to prepare thermodynamically metastable materials.

Although soft chemical synthesis using topotactic reactions has been developed on powder samples, thin films possess potential advantages over bulk studies, such as enhanced reactivity and high crystallinity. For example, it was reported that the topotactic reaction between $SrFeO_{2.5}$ thin films and polyvinylidene fluoride proceeds at much lower temperature than bulk powder. However, most of the topotactic studies on thin films focused on preparation of already reported materials rather than exploration of novel materials. Thus, in this thesis, I explored topotactic reactions on transition-metal oxide thin films to prepare novel oxide-based materials. In particular, I used anion exchange and insertion reactions to control the structures and properties of perovskite nickel oxides and copper oxides.

2. Synthesis of defect-fluorite $NdNiO_xH_y$ from $NdNiO_3$ precursors

First, I chose perovskite $NdNiO_3$, which shows temperature-dependent metal–insulator transition, as a precursor material. Observation by scanning transmission electron microscopy revealed that by hydride (H^-) exchange reaction using CaH_2, a defect fluorite structured phase was obtained as thin films on $SrTiO_3$ substrate, as shown in Figure 1. This phase was identified as new oxyhydride $NdNiO_xH_y$. This is in contrast to previous literature on the reaction using powder samples of $NdNiO_3$, where only oxygen deintercalation and not hydride incorporation took place. Furthermore, the epitaxial relation of the fluorite phase to the substrate could be changed by reaction conditions. When the reaction was performed at 240 °C, I obtained [001] oriented growth with a thin layer of oxygen-deficient phase $NdNiO_2$ at the interface between the film and the substrate. On the other hand, at higher temperature of 400 °C, [110]-oriented $NdNiO_xH_y$ film was obtained without $NdNiO_2$.

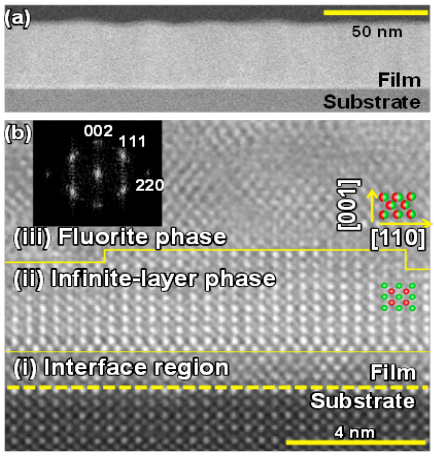

Figure 1. (a) Wide and (b) magnified views of HAADF-STEM images after reacting $NdNiO_3$ and CaH_2 at 240 °C for 12 h. Inset shows Fourier transform of the region (iii). Reprinted from Daltron Transactions, **30**, 12114 (2016), licensed under CC BY 3.0, Copyright 2016 the Royal Society of Chemistry.

3. Reversible changes in resistance of perovskite nickelate $NdNiO_3$ by fluorine substitution

Next, with the same starting material of $NdNiO_3$, I performed topotactic fluorination using polyvinylidene fluoride (PVDF). Though H^- and F^- possess the same formal valence and similar ionic radius, the reactions of $NdNiO_3$ with CaH_2 and PVDF proceeded very differently. That is, the

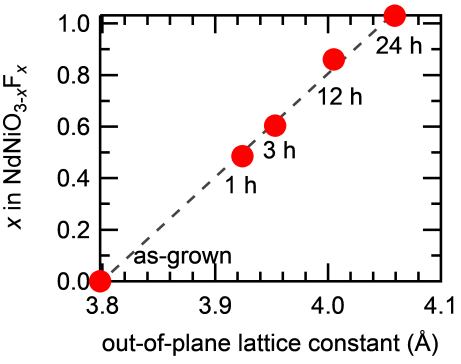

Figure 2. Relationship between fluorine contents x and out-of-plane lattice constants of $NdNiO_{3-x}F_x$ thin films prepared by PVDF fluorination. Reprinted with permission from ACS Applied Materials & Interfaces, **9**, 10882 (2017), Copyright 2017 American Chemical Society.

perovskite framework was completely maintained throughout the reaction, and perovskite oxyfluoride $NdNiO_{3-x}F_x$ was formed. As shown in Figure 2, the fluorine content x inside the film was systematically controlled by the reaction time with PVDF. The fluorinated films were highly insulating in contrast to $NdNiO_3$ with metallic conduction, and showed a bandgap of up to 2.1 eV. Hard X-ray photoelectron and soft X-ray absorption spectroscopies were performed to investigate the electronic states of the obtained films. They revealed the suppression of the density of states at the Fermi level as well as electron doping into nickel ions. The changes in the spectra indicated that the insulating characteristics of the $NdNiO_{3-x}F_x$ thin films were induced by Mott transition as a result of change in nickel valence states. Furthermore, I also found that the fluorine ions incorporated into the films could be removed by annealing under oxygen atmosphere, yielding the original $NdNiO_3$ with metallic conduction.

4. Fluorination of perovskite cuprate $LaCuO_x$ thin films

Like $NdNiO_{3-x}F_x$, most of the transition-metal oxyfluorides with perovskite (ABX_3) structure are insulating because of the strong ionicity of metal-fluorine bonds. To obtain conducting oxyfluorides with perovskite structure, I chose another starting material, $LaCuO_x$. Since some copper oxyfluorides with 2 $\pm$ δ valence states, such as $Sr_2CuO_2F_{2+x}$ show high-temperature superconductivity, I supposed that conducting materials could be obtained by synthesizing oxyfluoride $LaCuO_xF_y$. By using CuF_2 as a fluorine source, fluoride ions were successfully introduced into the $LaCuO_x$ films. Figure 3 shows temperature dependence of resistivity of the films before and after fluorination. Although the sample contained spatial inhomogeneity in

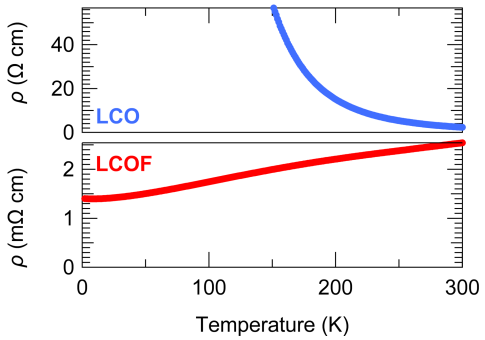

Figure 3. Temperature dependence of resistivity of $LaCuO_x$ and $LaCuO_xF_y$ thin films.

chemical composition, the fluorinated $LaCuO_xF_y$ film showed metallic conduction with resistivity of the order of mΩ cm at 300 K.

5. Conclusion

In conclusion, I performed different soft chemical processes on two different transition-metal oxide thin films, $NdNiO_3$ and $LaCuO_x$. The results revealed that introduction of F and H into thin-film samples could drastically alter their crystal structures and/or electrical transport properties. These methods are a promising way to synthesize new materials containing multiple anions and to modify the physical properties of oxide materials.

Acknowledgement

It has been six years since I joined the Hasegawa group. Looking back on days I spent in this laboratory, I cannot help but realize how much support I got to come through by now.

First of all, I would like to show my greatest appreciation to my supervisor, Prof. Tetsuya Hasegawa, who gave me an invaluable opportunity to study in this laboratory. Not only did he arrange the optimum environment for conducting research activities, he has always done every possible measure so that we can have a comfortable life in the laboratory. He always provided me with insightful suggestions whenever I had a research discussion with him, prepared for a conference, or wrote an application for grant. I am sure this thesis would not have been possible without his tremendous support.

I would also like to thank Prof. Tomoteru Fukumura in Tohoku University for his illuminating advice. His deep knowledge and clear comments helped me proceed my projects. I am also impressed by his passion for research.

As a member of Chikamatsu Group, I owe a very important debt to Assistant Prof. Akira Chikamatsu, who offered this challenging and intriguing project. I had a myriad of talks with him, ranging from deep research discussions to casual chatting. I remember that any papers or abstracts submitted to him return with corrections so many that they looked almost completely in red. Furthermore, whenever I felt stuck at my work, it was always his warm, kind encouragements that cheered me up.

I would also like to express my gratitude to Associate Prof. Yasushi Hirose. Prof. Hirose gave me a lot of useful information about experimental techniques. I never received his comments without being amazed at his broad, profound expertise. I cannot count how many times I consulted him about what kind of process would be best to achieve my goal, and his advice has always been reliable.

Secretaries in our lab, Ms. Mie Umino, Ms. Miki Komazawa, and Ms. Aya Imoji supported numerous things such as purchase of stuffs, preparation for my official trips. I also thank to researchers in the lab, Mr. Shoichiro Nakao, Dr. Sohei Okazaki, and Dr.Yang Chang, for supporting my research life.

Hasegawa lab is full of marvelous colleagues. It was all thanks to them that I could spend years enjoying lab works. Especially, Dr. Kei Shigematsu and Dr. Tsukasa Katayama took enormous care of me. They supported my using every single research equipment with great patience. They never hesitated to help proof my résumés. They told me how to proceed a project. Their attitude to research gave me a sense of what a scientist should be, without words.

I am grateful for other Chikamatsu group members, Mr. Keisuke Kawahara, Mr. Fahd Kahn Sikandar, Mr. Ryota Kantake, Mr. Yuji Kurauchi, Mr. Keisuke Yamada, Mr. Takaaki Shiina, Mr. Takahiro Maruyama, Mr. Kuni Yamada, Mr. Takuya Sahashi, Mr. Ryosuke Ishigami, and Mr. Gu Ke. While I was teaching them as a senior student, they taught me a lot. I would also like to show my gratitude for other colleagues and former colleagues, Dr. Anri Watanabe, Dr. Daichi Oka, Dr. Shungo Kojima, Dr. Jie Wei, Dr. Thantip S. Krasienapibal, Dr. Atsushi Suzuki, Dr. Mayuko Oka, Dr. Ryosuke Sei, Mr. Yutaka Uchida, Mr. Dai Kutsuzawa, Mr. Takanori Yamazaki, Mr. Naoki Kashiwa, Mr. Shunsuke Shibata, Mr. Naoaki Hashimoto, Dr. Youngok Park, Dr. Daisuke Ogawa, Mr. Ryosuke Takagi, and Ms. Kaori Kurita, Mr. Takuma Takeda, Mr. Masato Tsuchii, Mr. Kento Magara, Mr. Takuto Wakasugi, Mr. Shishin Mo, Mr. Ken Hayahara, Mr. Shunya Tanaka, Ms. Yuting Zhu, Mr. Satoshi Fujiwara, and Mr. Michitaka Fukumoto for supporting through valuable comments in seminars, daily chatting, and technical assistance.

I was supported by Japan Society for the Promotion of Science through Program for Leading Graduate Schools (MERIT). Especially, I want to thank Associate Prof. Kyoko

Ishizaka in the Department of Applied Physics for being my sub supervisor. Every time I had a discussion with her, I was enlightened to hear her elucidating viewpoints as a physicist. She kindly prepared an opportunity to discuss with members in her lab, which gave new insights to me.

Finally, my heartfelt appreciation goes to my family. Thanks to their support, I was able to spend years as a master course student without getting any serious illnesses. In these days, I recognized how precious the support from my family is. There is no place I'd rather be than with family!

Conducting scientific research is a fun but tough thing. It is not always successful, and no one knows when it bears fruit. This Ph. D course was so demanding for me that I almost wanted to quit many times. In such times, all the people surrounding me reminded me of a delight to do research. How lucky I am to be in such a wonderful environment! I cannot find words to express my gratitude to all the people that cared me.

December, 2017

Tomoya ONOZUKA

Contents

Chapter 1. General introduction

1.1 Soft chemical methods for metal oxides

Transition-metal oxides show a wide variety of physical properties such as magnetism, metal–insulator transition, ferroelectricity, and superconductivity [1]. These properties arise from the rich structural chemistry and partially-filled metal d orbitals. The synthesis and investigation of these materials have therefore been extensively studied by chemists as well as physicists and engineers.

The most traditional and basic approach for control of properties of transition-metal oxides is elemental substitution, where a part of the constituent chemical elements in a parent compound is substituted by other elements. A classic example is high-temperature superconductivity in a copper oxide system, $La_{2-x}Sr_xCuO_4$. As shown in a phase diagram in Figure 1-1, the parent compound of this system, La_2CuO_4, is an antiferromagnetic insulator. However, after partial substitution of strontium for lanthanum, the material shows superconductivity with maximum transition temperature of ~ 40 K. Another renowned system is perovskite manganites, $La_{1-x}Sr_xMnO_3$. Similarly to La_2CuO_4, $LaMnO_3$ is an insulator with magnetic ordering. Upon hole doping by strontium substitution, complex exchange interaction in manganese atoms results in ferromagnetic ordering (Figure 1-2), instead of superconductivity in cuprates. In perovskite manganites, electrical conduction and magnetism are closely coupled via so-called double exchange mechanism. As a result, colossal magnetoresistance, where the conductivity of the sample decreases by several orders of magnitudes under applied magnetic field, manifests itself in $La_{1-x}Sr_xMnO_3$.

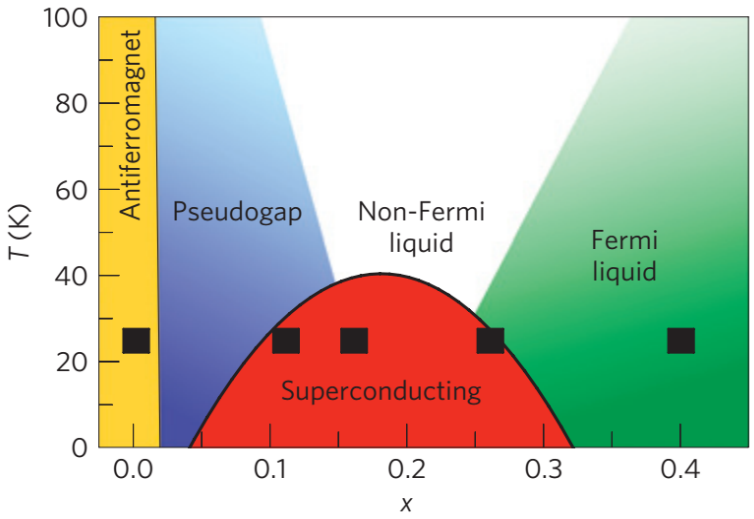

Figure 1-1 A schematic phase diagram for $La_{2-x}Sr_xCuO_4$ as a function of x. Reprinted by permission from Macmillan Publishers Ltd: Nature Materials Ref [2], copyright 2013.

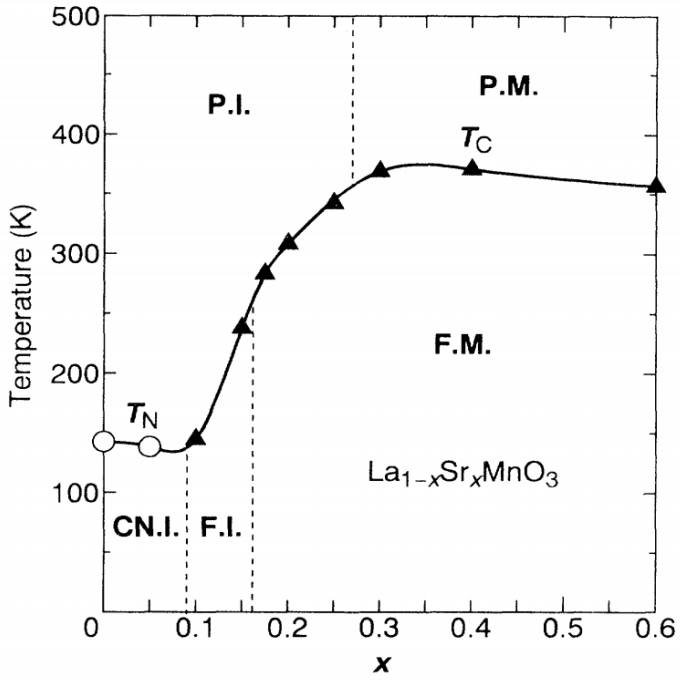

Figure 1-2 Electronic phase diagram of $La_{1-x}Sr_xMnO_3$. P.I.: paramagnetic insulator; P.M.: paramagnetic metal; CN.I.: spin-canted insulator; F.I.: ferromagnetic insulator. F.M.: ferromagnetic metal. Reprinted with permission from Ref [3] Copyright 1995 by the American Physical Society.

In both of the above two systems, the physical properties were controlled by substitution of metal ions. Actually, control of properties through metal ions, or cations, is much more commonly performed than through anions. This is understandable, considering how these materials are typically prepared. In conventional solid-state synthesis or the "shake-and-bake" method, a mixture of several metal oxides and/or metal oxy-acid salts (carbonates, nitrates, etc.) is sintered to obtain a complex transition-metal oxide. Especially, metal oxides have high lattice energy and melting points, which indicates the existence of a rigid framework comprising metal cations and oxide anions. To break that rigid network, an extremely high temperature (T > 1000 °C) compared to those of typical liquid- and gas-phase reactions is often required.

One disadvantage of this method is its thermodynamic nature. The thermal energy given during the reaction is sufficiently large, and it will exceed activation energies of all the possible competing reactions. In such a case, only the phase with the lowest free energy would remain after completion of the reactions. As a consequence, most of metastable product phases are hard to synthesize through this process.

To overcome this disadvantage, several synthetic strategies that can "soften" the process (i.e. lower the reaction temperature) have been developed so far. These methods are called soft chemical methods as opposed the conventional (hard) solid state synthesis. They can be divided into three major groups:

1. Co-precipitation or sol-gel methods to improve the mixing and/or reduce the particle size of starting materials.
2. Solvothermal or flux synthesis to lower the energetic barriers to diffusion.
3. Topotactic reactions, where the initial framework of the crystal structure is maintained during the reaction.

Among them, the topotactic reactions are peculiar in that they are rather *kinetic* processes. Figure 1-3 shows various examples of topotactic reactions. In many complex

metal oxides, a group of ions (typically light elements such as H, Li, Na, O, F) are often far more mobile than other host ions even at sufficiently low temperature. Exploiting this high mobility, one can selectively substitute, exchange, intercalate, or extract those components while maintaining the basic structural topology. This conservation of the structure during synthetic process allows a flexible design of a target material that is metastable and cannot be formed at elevated temperature. Furthermore, in transition-metal oxides, oxygen is usually the element with highest mobility; thus, the topotactic reactions are effective in the control of oxide ions i.e. anions.

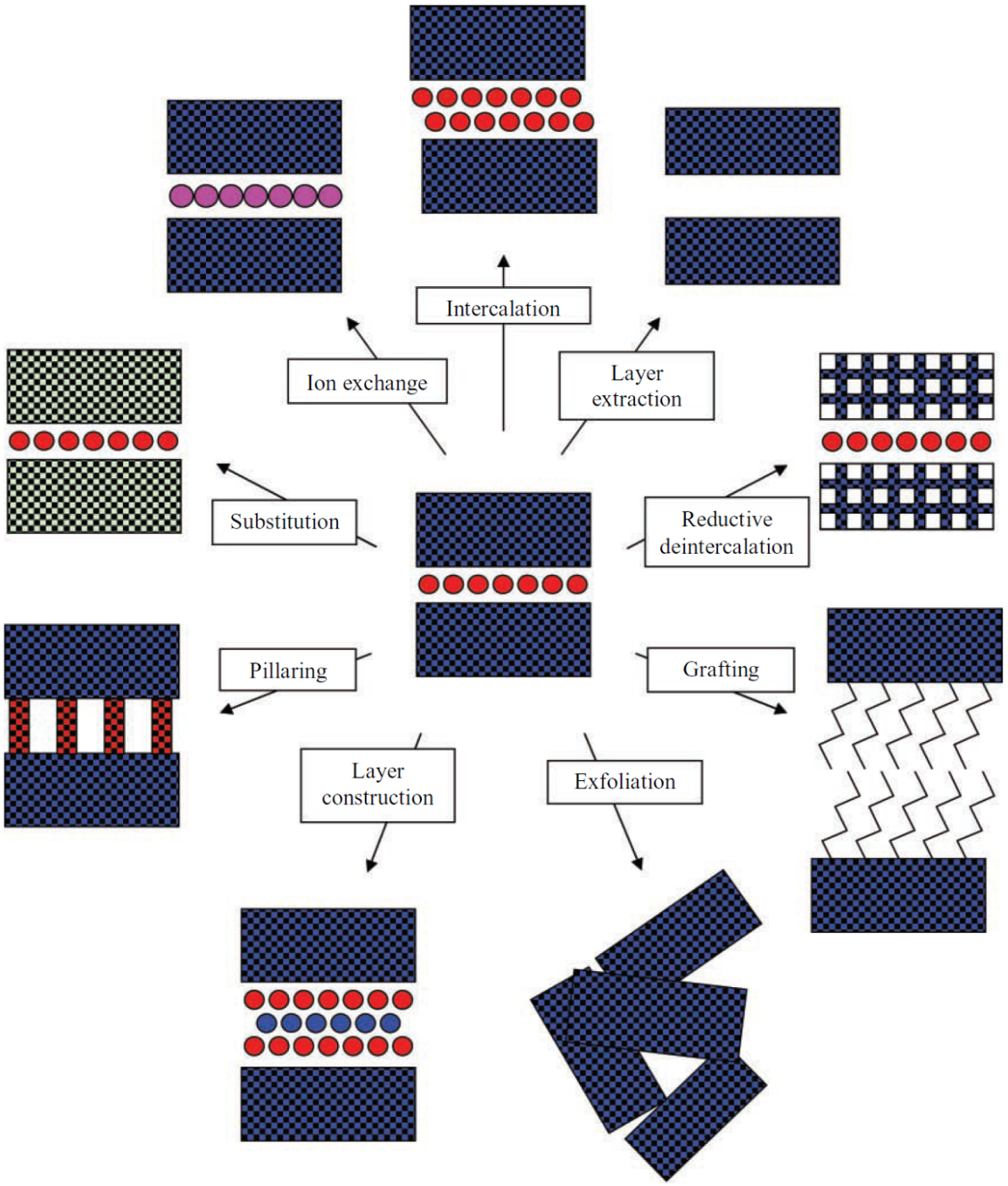

Figure 1-3. Examples of topotactic reactions. Reprinted with permission from Ref [4]. Copyright 2011 by John Wiley and Sons)

The topotactic reactions have two aspects: the crystallographic and the chemical change. The former represents what kind of topological change occurs, which includes substitution, insertion, and extraction. The latter is associated with the change of the

valence state of a particular element; it can be oxidative, reductive, or charge-neutral. Those two factors are closely related to each other. For example, if an anion is inserted into the host compound, this reaction is oxidative insertion, but if it is substituted for a part of the sites, it will become reductive, oxidative or redox-neutral substitution depending on the chemical valence of the two ions. Examples of these different reactions are as follows:

Reductive insertion [5]: $LiCa_2Ta_3O_{10} + C_4H_9Li \rightarrow Li_2Ca_2Ta_3O_{10}$

Reductive extraction [6]: $LaNiO_3 + NaH \rightarrow LaNiO_2$

Oxidative insertion [7]: $A_2LaNb_2O_7 + Cl_2 \rightarrow A_2ClLaNb_2O_7$ (A = Cs, Rb)

Oxidative extraction [8]: $LiCoO_2 \rightarrow Li_{1-x}CoO_2 + xLi$

Redox-neutral insertion [9]: $Bi_2Sr_2CaCu_2O_y + Ag + I_2 \rightarrow AgIBi_2Sr_2CaCu_2O_y$

Redox-neutral extraction [10]: $K_2La_2Ti_3O_{10} + PPh_4Br \rightarrow La_2Ti_3O_{10}$

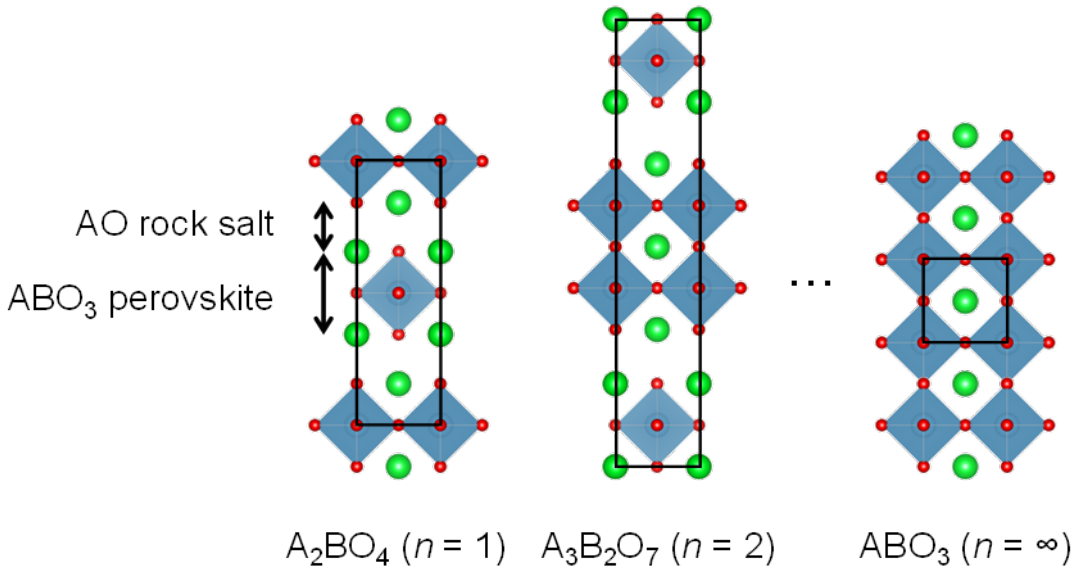

Figure 1-4. Ruddlesden–Popper (RP) layered perovskite $A_{n+1}B_nO_{3n+1}$. Red, green, and blue spheres represent O, A, B atoms, respectively. (This and following figures of crystal structures were drawn with VESTA3 [11].) The unit cell of each compound is represented by a black frame.

How an actual reaction proceeds is thus determined by both the crystal structure and the chemical properties of the host material. Here, I will take Ruddlesden–Popper (RP) layered perovskite system, $A_{n+1}B_nO_{3n+1}$ as an example. As shown in Figure 1-4, a RP perovskite consist of alternating stacks of AO rock salt and ABO_3 perovskite blocks. The parameter *n* represents the number of consecutive blocks. It is noteworthy that these two components often react differently. As shown in Figure 1-5, the rock salt blocks in RP perovskites contain tetrahedral interstitial sites, indicating that the insertion of other chemical species is likely to occur. In fact, several complex oxides with excess anions such as La_2MO_{4+x} (*M* = Ni; Co; Cu) [12–14], $La_2CuO_4F_x$ [15], $Sr_3Ru_2O_7F_2$ [16], $La_{1.2}Sr_{1.8}Mn_2O_7F_2$, La_2MnO_4F [17], and $Sr_2CuO_2F_{2+x}$ [18] have been synthesized in a topotactic manner. On the other hand, simple perovskite can be regarded as a RP perovskite with $n = \infty$, and it does not contain any AO rock salt layers. Thus, topotactic insertion into ABO_3 is not observed, and substitution or deintercalation is more likely to occur.

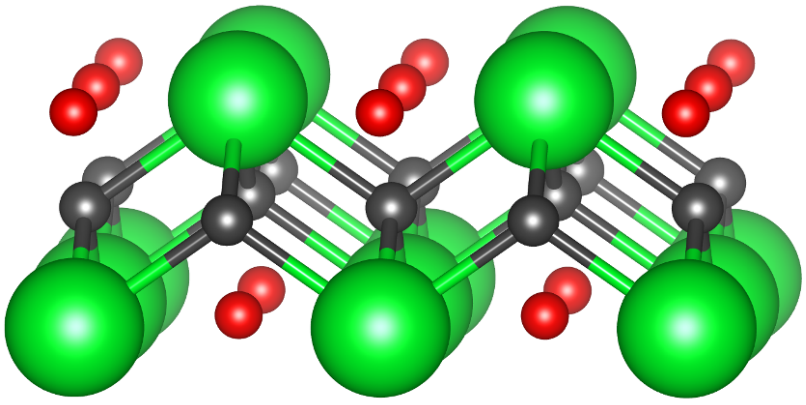

Figure 1-5. Interstitial sites (gray spheres) contained in a rock-salt block of RP perovskites.

1.1.1 Reactions using molecular hydrogen and metal hydrides

Deintercalation of oxygen

By topotactic deintercalation of oxygen from host complex oxides, it is possible to synthesize metastable oxides with unusual coordination numbers and/or chemical valence state. For example, topotactic reduction of $CaMnO_3$ leads to oxygen-defect perovskite $CaMnO_{2.5}$, according to the following reaction at 300 °C:

$$CaMnO_3 + xH_2 \rightarrow CaMnO_{3-x} + xH_2O$$

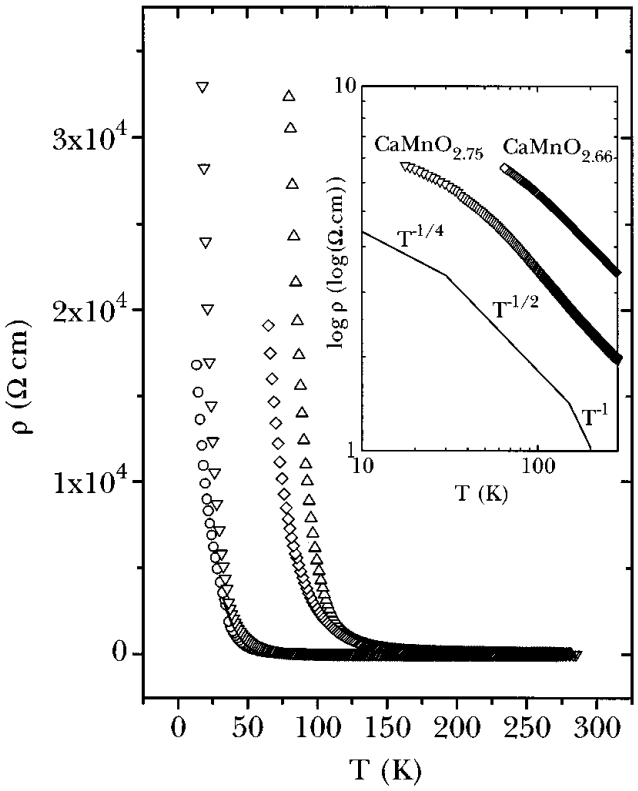

Figure 1-6. Electrical resistivity vs. temperature of (△) $CaMnO_3$, (○) $CaMnO_{2.84}$, (▽) $CaMnO_{2.75}$, and (◇) $CaMnO_{2.66}$. Reprinted with permission from Ref. [19]. Copyright 1996 by the American Physical Society.

Oxygen-deficient $CaMnO_{3-x}$ exhibits unusual physical properties, commonly seen in many topotactically reduced materials. The end member $CaMnO_3$ ($x = 0$) is an antiferromagnetic insulator or so-called Mott insulator, an energy gap opens at the Fermi

level because of strong Coulomb repulsion between electrons. Introducing oxygen vacancies into it causes electron doping. Figure 1-6 shows electrical resistivity of $CaMnO_{3-x}$ with different x values. Notably, the resistivity shows insulating behavior ($d\rho/dT < 0$) in all the x range from 0 to 0.34, in stark contrast to isoelectronic $La_{1-x}Ca_xMnO_3$, in which metallic transport and complex magnetic order are observed depending on x [1]. Several mechanisms have been proposed to explain this insulating behavior such as localization of doped electrons by the random potential of oxygen vacancies, and inhibition of carrier delocalization by poor orbital overlap between Mn and O originating from deviation of Mn−O−Mn bond angle from 180° [20].

Chemical reduction by hydrogen gas can provide a variety of oxygen-deficient perovskites, but there are several potential drawbacks in this method. Firstly, the reactivity of H_2 gas is limited because enough energy must be added to break H−H bonds. As a result, the reaction temperature should be above 300 °C, making it impossible to obtain metastable phases that decompose at such high temperature. Another potential drawback is the formation of H_2O molecules accompanied with the reaction. Some oxides, such as Hg-based cuprates, degrade when exposed to moisture-containing air [21], and such water-sensitive materials are difficult to be synthesized by H_2 reduction. Crespin et al. [30] examined topotactic reduction of $LaNiO_3$ with H_2 to obtain that infinite-layer $LaNiO_2$ (Figure 1-7). Infinite-layer $LaNiO_2$ has a layered structure with unusually low Ni^+ valence state (d^9 electron configuration), similar to high-temperature cuprate superconductors. They succeeded in synthesizing infinite-layer $LaNiO_2$ but they have to use a complex gas recirculating system as shown in Figure 1-8, to trap all gaseous reaction products and introduce fresh hydrogen gas. This complex apparatus prevented other researchers from reproducing reliable synthesis of this material [22,23].

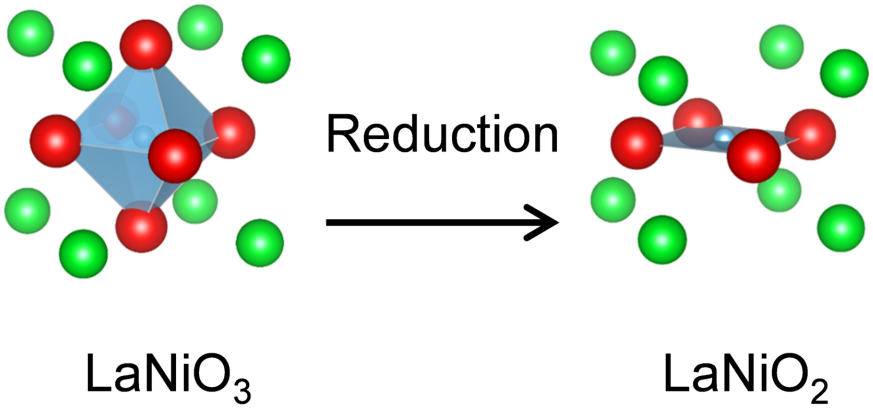

Figure 1-7. Synthesis of infinite-layer $LaNiO_2$ through topotactic deintercalation of oxygen.

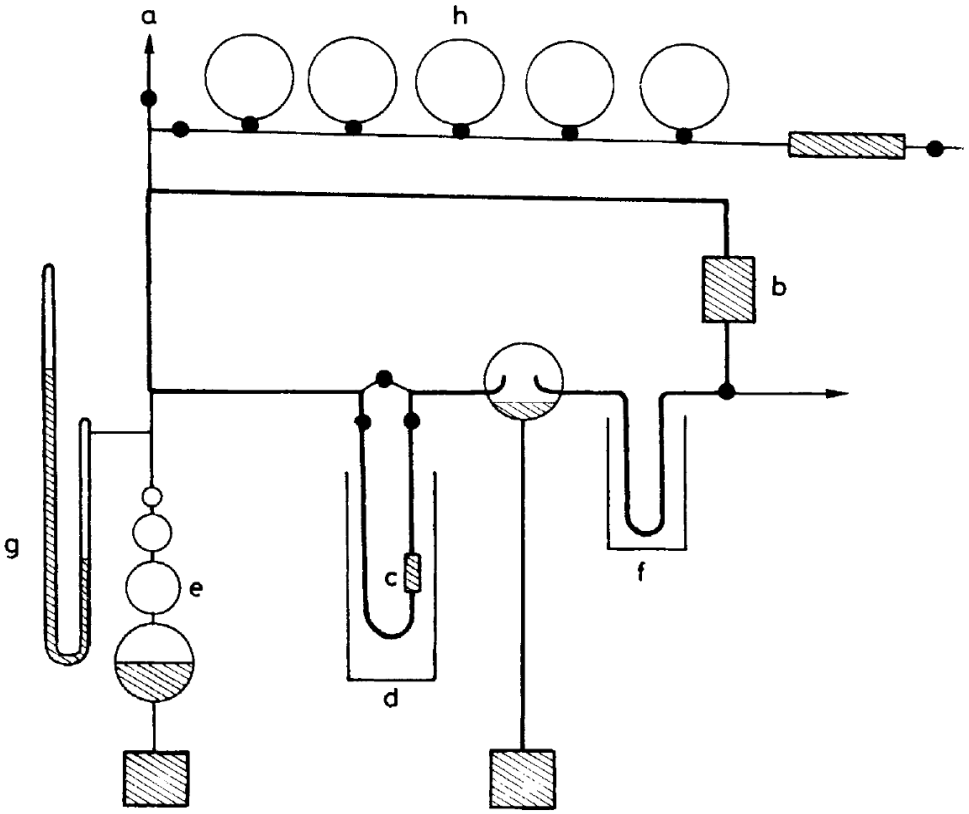

Figure 1-8. Apparatus for circulating hydrogen gas used for the synthesis of $LaNiO_2$. The chemical reaction takes place at reactor (c), enclosed in an electric furnace (d). Reproduced from Ref [24] with permission of The Royal Society of Chemistry.

One way to address these problems is to use metal hydrides such as NaH [6],

CaH_2 [25], and LiH [26]. The reactions are described by the following formulas:

$$LaNiO_3 + NaH \rightarrow LaNiO_2 + NaOH$$

$$Y_2Ti_2O_7 + xCaH_2 \rightarrow Y_2Ti_2O_{7-x} + xCaO + xH_2$$

$$Ba_{0.5}Sr_{0.5}MnO_{3-x} + 2yLiH \rightarrow Ba_{0.5}Sr_{0.5}MnO_{3-x-y} + yLi_2O + yH_2$$

High thermal stability of NaOH, CaO, Li_2O is the driving force of these reactions. In these reactions, H_2O was not formed after reaction in contrast to reduction using H_2 gas. In addition, metal hydrides are generally stronger reducing reagents than hydrogen gas, enabling introduction of a larger amount of oxygen vacancies than H_2. Indeed, above-mentioned infinite-layer $LaNiO_2$ was synthesized with good reproducibility by using NaH as a reducing agent. Another example of exotic materials is infinite-layer $SrFeO_2$. It can be synthesized topotactically from $SrFeO_{2.5}$ at 280 °C with CaH_2 as a reducing agent [27]. In $SrFeO_2$, iron possesses 2+ valence states with unusual square-planar coordination. In general, square-planar coordination appears when the central metal ion is Jahn–Teller active (such as d^9 in Cu^{2+}). However, the d^6 electron configuration of Fe^{2+} is not considered as Jahn–Teller active, which makes its existence puzzling. $SrFeO_2$ is an antiferromagnetic insulator with $T_N = 473$ K; carrier-doping into this material may realize novel transport phenomena such as superconductivity.

Three metal hydrides NaH, CaH_2, and LiH have different usages. NaH is used at relatively low temperature (≥ 150 °C), but it cannot be used at elevated temperature (> 225 °C). At higher temperature, CaH_2 is useful because it can survive up to 885 °C. Usage of LiH is more specialized than the other two. In general, after the reaction, residual oxides or hydroxides (NaOH, CaO, and Li_2O) is washed out using organic solvents or weak acids. In the topotactic reduction of $Ba_{0.5}Sr_{0.5}MnO_{3-x}$, however, washing NaOH with methanol resulted in decomposition of the product. Washing the reaction products obtained from LiH did not cause such decomposition [26].

The reaction mechanism of topotactic reduction with metal hydride has yet to be

fully understood. Originally, it was reported [6] that intimate contact with NaH is required for the synthesis of $LaNiO_3$ powder, suggesting importance of ionic diffusion between the two materials. Other researchers, however, reported that topotactic reduction of bulk $SrFeO_3$, thin film $SrFeO_{2.5}$, and thin film $LaNiO_3$ proceeded even when the oxides and CaH_2 were physically separated against each other [28], maintaining that H_2 gas released from metal hydrides plays a main role in these materials.

Synthesis of mixed oxyhydrides

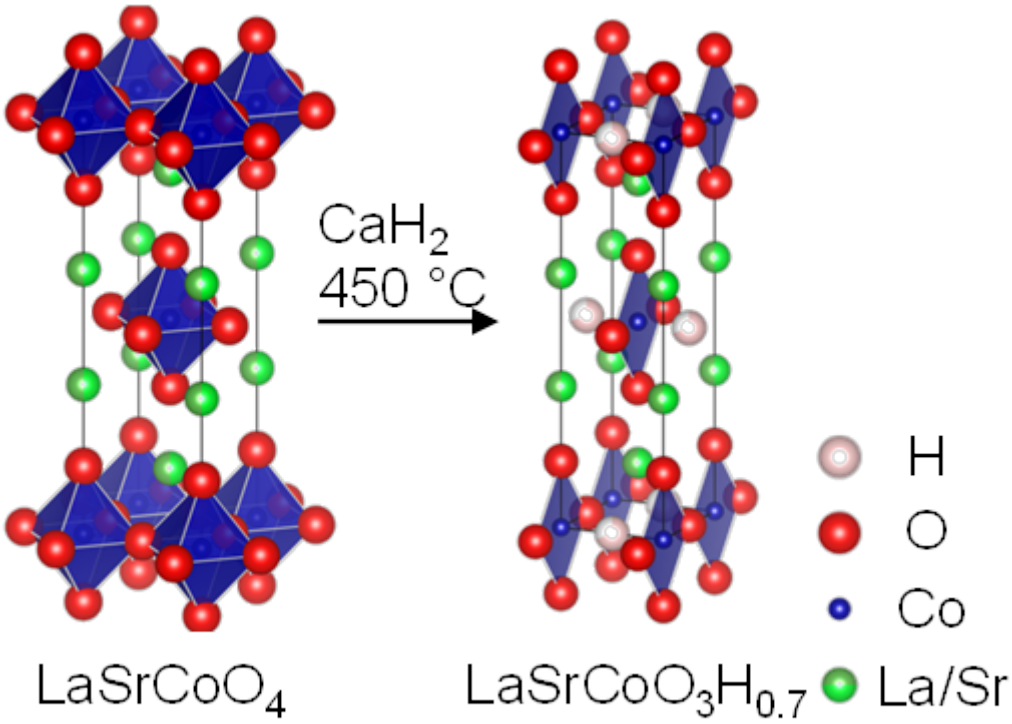

Figure 1-9. Topotactic synthesis of oxyhydride LaSrCoO3H0.7 [29]

In the previous section various examples of oxygen deintercalation were described. In some materials, however, another type of reactions occurs. For example, reaction of RP perovskite $LaSrCoO_4$ with CaH_2 at 450 °C produces oxide hydride $LaSrCoO_3H_{0.7}$, where O^{2-} and H^- ions coexist in a single material. As shown in Figure 1-9, O^{2-} and H^- are ordered, forming Co–O one-dimensional chains bridged by H^- anions. This

compound shows antiferromagnetic transition at 380 K, which is much higher than that of $LaSrCoO_{3.5}$ (110 K) with a similar concentration of "bridging" anions (0.7 vs. 0.5). The high Néel temperature of $LaSrCoO_3H_{0.7}$ indicates that H^- anion is able to magnetically couple with transition metal ion at least as strong as O^{2-} is.

For stable formation of oxyhydrides, it is important to suppress several H^--consuming reactions such as [30]:

$$2\ H^- + 0.5\ O_2 \Leftrightarrow H_2 + O^{2-},$$

$$2\ H^- + M^{n+} \Leftrightarrow H_2 + M^{(n-2)+},$$

$$H^- + H_2O \Leftrightarrow H_2 + OH^-.$$

These equilibria should be displaced to the left in order to stabilize H^- species in oxides. The first reaction demonstrates that H^- ions are stable in a strongly reducing environment. Usage of metal hydrides rather than hydrogen gas is desirable due to its strong reducing ability. The second reaction represents reduction of transition-metal ions by H^-. This indicates that the cations of electropositive main-group element such as rare earths, and transition-metal cations with the lowest possible valence state are candidate components of oxide hydrides. The third one describes that moisture may hinder the formation of oxide hydrides and thus it should be removed from the reaction atmosphere. Again, metal hydrides are superior in this regard to hydrogen gas because they can strongly absorb moisture.

Table 1-1. List of oxyhydrides with perovskite-related structures synthesized by topotactic methods.

Product	Valence	Precursor	Temperature	Reference
$LaSrCoO_3H_{0.7}$	$Co^{1.7+}$	$LaSrCoO_4$	450 °C	[29]
$Sr_3Co_2O_{4.33}H_{0.84}$	$Co^{1.75+}$	$Sr_3Co_2O_{7-x}$	255 °C	[31]
$ATiO_{3-x}H_x$ (A: Ca, Sr, Ba, Eu)	$Ti^{(4-x)+}$	$ATiO_3$	530–580 °C	[32–34]
$SrVO_2H$	V^{3+}	$SrVO_3$	600 °C	[35]
Sr_2VO_3H	V^{3+}	Sr_2VO_4	600 °C	[35]
$Sr_3V_2O_5H_2$	V^{3+}	$Sr_3V_2O_7$	600 °C	[35]
$SrCoO_2H$	Co^{3+}	$SrCoO_{2.5}$	250 °C	[36]

Table 1-1 lists oxide hydride materials synthesized through topotactic process. In $LaSrCoO_3H_{0.7}$ and $Sr_3Co_2O_{4.33}H_{0.84}$, the chemical state of cobalt is $Co^{1.7+}$ and $Co^{1.75+}$, respectively. On the other hand, in the rest of the materials in the table, the transition elements such as Ti and V did not possess the lowest possible oxidation state. The reason why H^- can coexist with the metal ions with relatively high valence is not completely clear; however, in transition-metal oxide hydrides, stronger covalency of the metal-hydrogen bonds than that in more ionic alkali and alkaline earth hydrides [37,38] and may stabilize H^- by decreasing the actual valence from −1. The hydride ions in perovskite oxide hydrides can be arranged in a highly ordered manner. Figure 1-10 shows different oxygen/hydrogen arrangements in three kinds of perovskite oxide hydrides. In $SrVO_2H$, H^- ions selectively occupy the apical sites of the vanadium ions, forming two-dimensional VO_2 layers analogous to superconducting cuprates. On the other hand, in perovskite chromate and titanate, H^- and O^{2-} are randomly distributed.

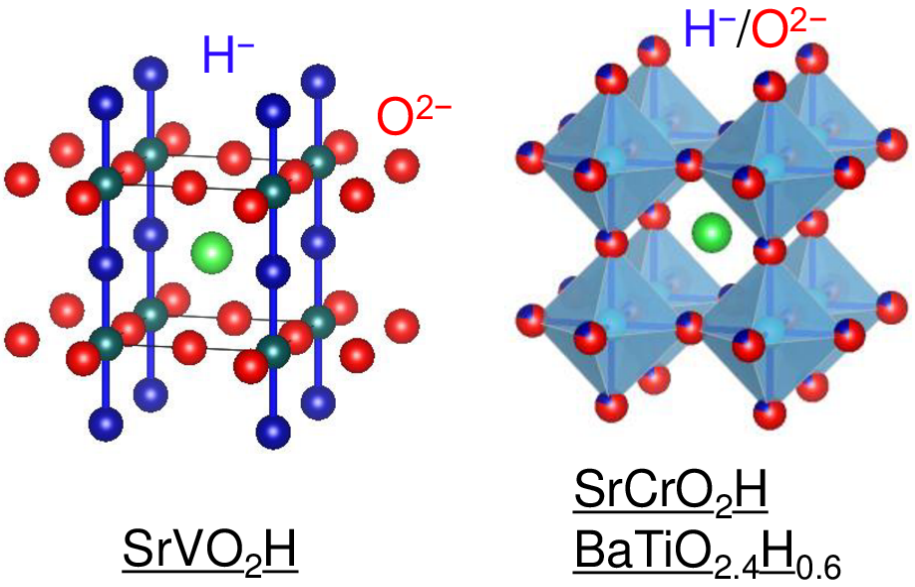

Figure 1-10. Arrangement of O^{2-} and H^{-} in three different perovskite oxyhydrides, $SrVO_2H$, $SrCrO_2H$, and $BaTiO_{2.4}H_{0.6}$.

1.1.2 Fluorination reactions

Since the ionic radii of F^{-} (133 pm) and O^{2-} (140 pm) are close to each other and −1 is the only stable chemical valence of fluorine (hydrogen can take +1, 0, or −1 states in solids), numerous oxide fluorides have been reported so far, most of which were obtained by topotactic fluorine introduction. For example, $Sr_2CuO_2F_{2+\delta}$ can be synthesized by treating precursor Sr_2CuO_3 with F_2 gas at 210 °C [18]. Excess fluorine located in the interstitial sites inside the SrO rock salt blocks (Figure 1-5) releases hole carriers, inducing superconductivity with maximum T_c of 46 K.

Although F^{-} itself is chemically stable, complex mixed oxide fluorides are often metastable and decompose at elevated temperature. Main decomposition products from perovskite and RP perovskite oxide fluorides are binary metal fluorides such as SrF_2 and rare earth (*R*) oxide fluorides *R*OF. High-pressure synthesis is a commonly used route for obtaining oxide fluorides [39,40], but it requires a specially-designed apparatus. Meanwhile, topotactic fluorination can be performed at lower temperature and the experimental setup is rather simple. Various fluorination reagents have been developed to

prepare impurity-free oxide fluoride samples [41,42], such as F_2, NH_4F, XeF_2, CuF_2, ZnF_2, polyvinylidene fluoride (PVDF), and polytetrafluoroethylene (Teflon®). Fluorination using electrochemical method has also been investigated [43,44].

Difference in reactivity among these reagents are as follows: F_2 gas is a highly oxidizing reagent, so it helps conduct fluorine insertion under highly oxidative conditions. The problem of F_2 gas is its high toxicity; special care must be taken for dealing with it. NH_4F and XeF_2 are less oxidizing than F_2, and thus allow fluorine substitution by keeping or lowering the oxidation state; however, they easily produce AF_2 and ROF (*A*: alkaline earth, *R*: rare earth) impurities. CuF_2 and ZnF_2 can be used without significant impurity formation, but CuO and ZnO are left in the sample. In 2002, Slater reported topotactic synthesis of $Sr_2TiO_3F_2$ and $Ca_2CuO_2F_2$ with NH_4F and PVDF [45]. In both compounds, the fluorination reaction with NH_4F produced binary fluoride as impurities (SrF_2 and CaF_2), whereas no impurities were formed with PVDF. Furthermore, PVDF as a fluorination reagent has other advantages: It is nontoxic solid and stable in air at room temperature; it has relatively low decomposition temperature (~ 200 °C) compared to inorganic reagents; it can perform reductive fluorination [41,46]. These properties enable us to perform fluorination of transition-metal oxides easily and safely.

1.2 Application to thin films

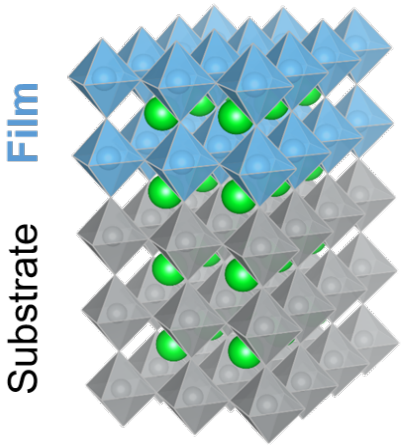

Figure 1-11. Schematic image of epitaxial growth.

Although soft chemical synthesis using topotactic reactions has been developed on powder samples, the method can also be applied to thin-film samples. In particular, use of epitaxially-grown films, in which the crystalline lattices are well aligned on single-crystalline substrate (see Figure 1-11), has several potential advantages.

First, with epitaxial growth one can obtain highly-crystalline samples with less grain boundary than powder samples, which are suitable for measurements of intrinsic physical properties, such as electrical conductivity [47,48]. This is especially useful for topotactically synthesized materials because low-temperature reaction of bulk samples often produces poorly-packed, coarse specimen with a large amount of grain boundaries and voids. In contrast, in the case of epitaxial thin films single-crystalline samples are more easily obtained owing to the epitaxial stabilization.

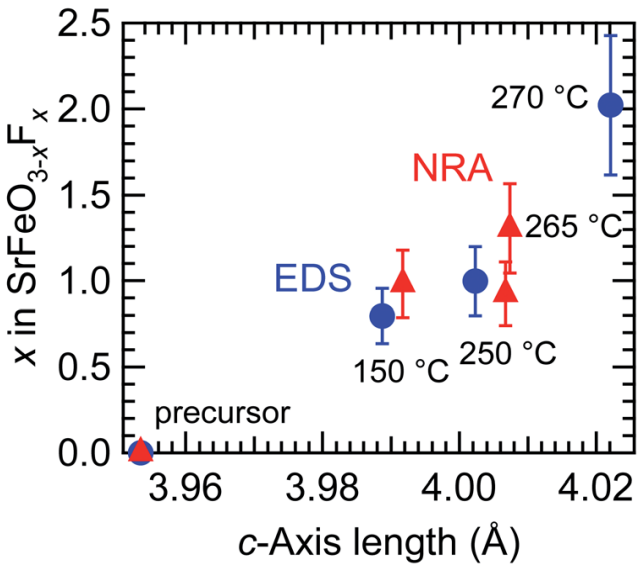

Figure 1-12. Fluorine content in $SrFeO_{3-x}F_x$ thin films reacted with PVDF at different temperatures. Note that fluorination starts at 150 °C, which is much lower than reaction temperature of bulk $SrFeO_3$ (400 °C). Reproduced from Ref [49] with permission of The Royal Society of Chemistry.

Another feature of thin films is their decreased dimension in the depth direction (~ 10^1 nm) as opposed to bulk (~ 1 μm), which leads to higher reactivity. For example, $SrFeO_{3-x}F_x$ thin films can be topotactically prepared from $SrFeO_{3-x}$ precursor at 150 °C [49], which is substantially lower than the reaction temperature for polycrystalline bulk $SrFeO_{3-x}$ (400 °C) [50]. Because of the higher reactivity, processing temperature can be lowered in thin films, which is helpful for obtaining metastable compounds which tend to decompose at elevated temperature.

Finally, thin films undergo artificial strain (epitaxial strain) from the substrate, which could result in unique structure and/or properties distinct from bulk samples. The epitaxial strain could provide an additional parameter that determines the structure after topotactic reactions, other than temperature, time, or reaction reagents. As shown in Figure 1-9, bulk $LaSrCoO_3H_{0.7}$ has certain pattern of O/H ordering, which resulted in an orthorhombic unit cell. Bouilly *et al.* tried to fabricate epitaxial thin film of this material on $LaSrAlO_4$ (LSAO) substrate, as shown in Figure 1-13 [51]. When it was grown in *a*-axis orientation

on LSAO (100) substrate, the film possessed orthorhombic structure similarly to the bulk sample, indicating O^{2-} and H^{-} ions are ordered in a similar manner to the bulk phase. In contrast, *c*-axis oriented $LaSrCoO_3H_{0.7}$ on LSAO (001) substrates possessed tetragonal symmetry. The authors attributed this to random distribution of O and H anions in the equatorial sites around Co ions, which is distinct from the bulk phase. Their results suggest that the manipulation of anion order in a topotactically synthesized mixed anion materials is possible by an appropriate choice of substrate orientation.

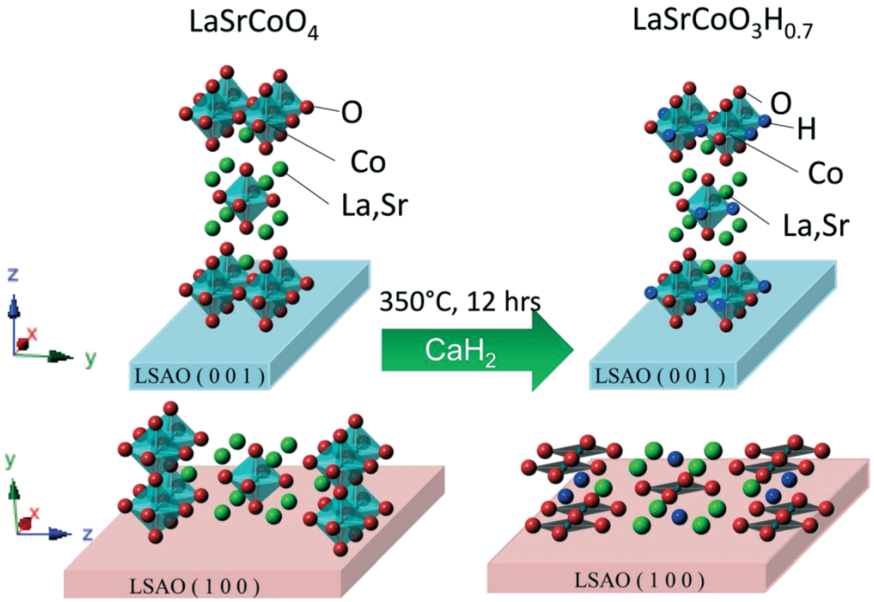

Figure 1-13. Topotactic conversion of the *c*-axis (upper) and a-axis (lower) oriented $LaSrCoO_4$ films on $LaSrAlO_4$ (LSAO) substrates. Reproduced from Ref [51] with permission of The Royal Society of Chemistry.

1.3 Purpose of this study

Transition-metal oxides exhibit a wide variety of interesting phenomena such as metal–insulator transition, ferromagnetism, and high-temperature superconductivity. Recently, synthesis of novel oxide-based materials by soft chemical methods has been vigorously studied because it could lower the reaction temperature and thus produce metastable compounds. Especially, use of epitaxial thin film samples is interesting because of enhanced reactivity of thin samples as well as other advantages, such as high crystallinity. However, previous studies on thin films rather focused on applying the methods for obtaining already-reported materials as thin films, rather than exploiting advantages of films to synthesize novel materials.

Thus, in this thesis work, I aimed to establish the combination of thin films and soft chemical methods as an effective approach for exploring novel inorganic materials and their physical properties. More concretely, I selected two transition-metal oxides, $NdNiO_3$ and $LaCuO_x$, as starting materials. With the aid of topotactic hydrogen substitution and fluorine substitution reactions, I tried to obtain novel mixed oxyhydride and oxyfluoride samples, and investigate their electrical properties.

Chapter 2. Experimental methods

2.1 Pulsed laser deposition (PLD)

2.1.1 General features of PLD

Pulsed laser deposition (PLD) is a physical vapor deposition process, where a target material is vaporized by a pulsed laser.

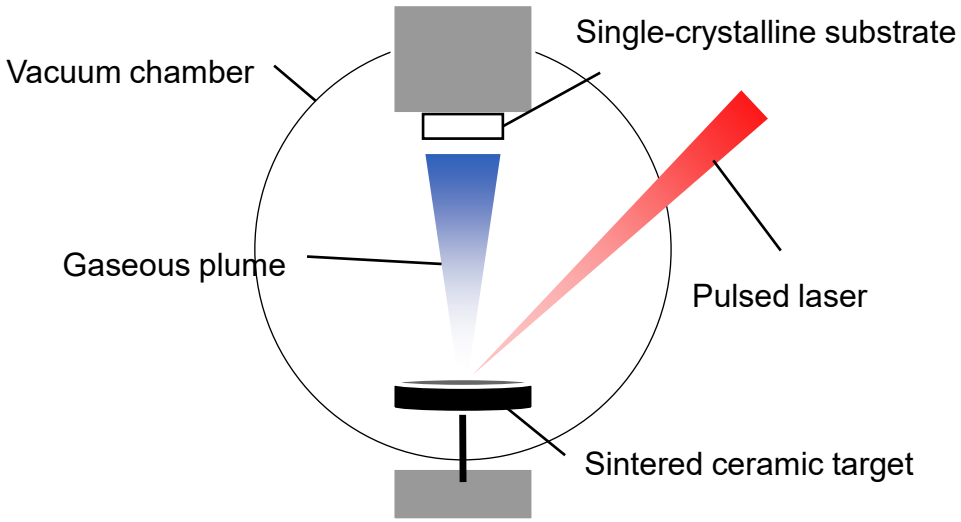

Figure 2-1. Schematic image of a typical PLD system.

Figure 2-1 shows a schematic image of a typical PLD system. A pulsed laser beam is focused onto a target, typically a sintered ceramic pellet, to ablate it into a plasma plume. Ultraviolet lasers such as KrF laser (248 nm) or fourth harmonic (266 nm) for Nd:YAG laser are commonly used so that enough energy is transferred onto the target. The ablated plasma flies basically in a straight direction to a substrate placed above the target, which can be heated by infrared lamp or diode laser heaters. The target and substrate are located inside an ultra-high vacuum (UHV) chamber with base pressure of 10^{-9}–10^{-8} Torr to eliminate contamination from atmospheric gases and particles. PLD has several

remarkable features that make it attractive for preparing various functional materials. They include [52]:

- Stoichiometric transfer from the target to the substrate
- Generation of energetic species
- Hyperthermal reaction between the ablated cations and the background gas in the ablation plasma
- Compatibility with background pressures ranging from ultrahigh vacuum (UHV) to 1 Torr.

The first feature, the stoichiometric transfer, would be one of the most important characteristics of PLD. The laser ablation process depends heavily on the laser energy. When the laser energy is sufficiently low, the vaporization of the target is simply a thermal process, i.e. the surface is heated by the laser to sublime into the chamber. In such cases, the composition of evaporated flux is dominated by vapor pressure of each element. In contrast, when the energy is increased above a certain threshold value which is determined by the absorption coefficient of the material, high density of energy is absorbed by a small volume of the material. Then the given energy is much larger than that required for vaporizing each element, which results in an ablation process that conserves stoichiometry between target and plume. Therefore, by appropriately choosing lasing conditions for a particular material, one can readily obtain multi-cation materials that possess the same cation composition as the target.

Availability of wide gas pressure range during deposition is also important. The introduced oxygen gas can serve as a part of the flux when depositing oxide materials. Thus, by changing the gas pressure and species inside the chamber, different phases would be formed. For example, to stabilize metal cations with unusually high oxidative state such as Ni^{3+}, high pressure of oxygen gas (> 100 mTorr) is required [53]. Another role of the gas is to reduce kinetic energies of the plume. Depending on lasing and gas

conditions, the kinetic energy can vary from 0.01–100 eV.

Since a highly-intensified laser is used to ablate a target, virtually almost all kinds of materials can be effectively transferred onto a substrate, except for wide-gap insulators with small optical absorption at the wavelength of the laser. Either polycrystalline ceramics or single crystals are available as targets. In general, the phase of the target need not be the same as that of the film to be deposited; only cation compositions are required to be identical between the two, because stoichiometric transfer is expected, as mentioned above. For ceramic targets, highly-dense sintered pellets are preferable because this will suppress formation of particles during ablation.

Optimization of the conditions of a substrate is also mandatory to fabricate high-quality films. Choice of the substrate itself is a critical parameter for film growth, because the crystalline lattice of the film tends to align reflecting that of the substrate. The difference of the lattice lengths between film and substrate must is often used as a parameter representing the lattice mismatch, given by

$$f = \frac{a_{\mathrm{film}} - a_{\mathrm{substrate}}}{a_{\mathrm{substrate}}},$$

where a_{film} and $a_{\mathrm{substrate}}$ represent the in-plane lattice constants of the film and substrate, respectively. If f is close to zero, the crystalline lattice of the film receives little strain and thus high crystallinity film can be obtained. On the other hand, if $|f|$ is too high, strains from the substrate become so large that the crystal relaxation occurs, or, in some cases, polycrystalline or amorphous thin film is formed. Under a moderate value of f, strain from the substrate remains in the film. This is the same as the situation that the crystal is subjected to external pressure, and in those films physical properties might be modified. Thin film growth is also affected by the crystal orientation of the substrate. For example, $SrTiO_3$, a typical substrate for growing perovskite thin films, has a cubic structure and substrates with three different orientations, (100), (110), and (111), are commercially

available. Substrate temperature is an important parameter governing thin film growth, as well. In general, too low substrate temperature tends to result in formation of amorphous films, while at too high temperature target materials may decompose.

To summarize, the following conditions are optimized to obtain high-quality thin films:

1. Lasing conditions (fluence, repetition rate)
2. Quality of a target (composition, sintered density, single or polycrystalline, etc.)
3. Chamber gas pressure
4. Substrate temperature
5. Lattice parameters and surface lattice plane of a substrate
6. Deposition time

2.1.2 PLD system used in this study

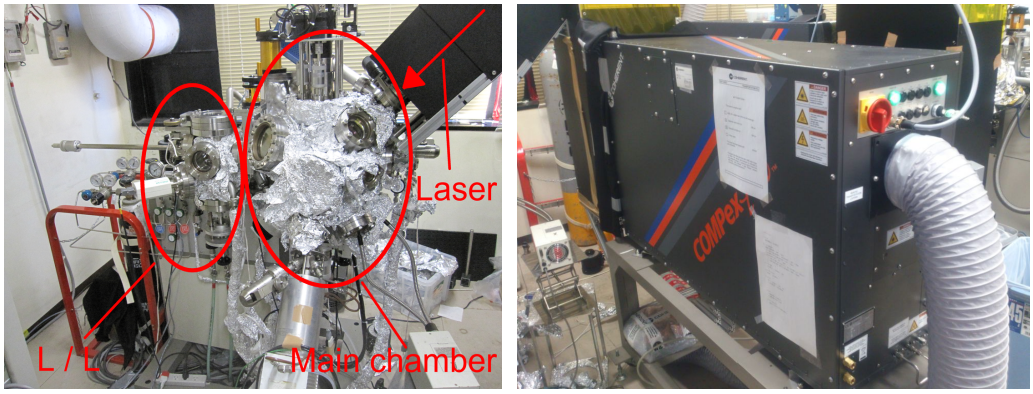

Figure 2-2. PLD system used in this study. Left: Main and Load/Lock chambers. Right: KrF excimer laser.

Figure 2-2 shows the PLD system used in this study. As seen in the left picture, the PLD is composed of two different vacuum chambers, Load/Lock (L/L) chamber and Main chamber. The L/L chamber is used for introducing and picking up samples, and the Main chamber for actual deposition. The two chambers are separated by a gate valve so that

one can introduce our samples without significant lowering of the vacuum level in the Main chamber. Pulsed laser beams are irradiated from the upper right box. The right figure in Figure 2-2 is a photo of the pulsed laser device. A KrF excimer laser with 248 nm wavelength is used. In KrF lasers, high voltage is applied to Kr/F_2 mixed gas. They react to form a temporary complex or an excimer:

$$2Kr + F_2 \rightarrow 2KrF$$

The excimer emits an ultraviolet photon when it decays to the ground state. Although Kr and F atoms constituting an excimer are bound together in the electronic excited state, they immediately dissociate after the emission of a photon. Therefore, inverted population between the excited and the ground state is easily realized, which is crucial to light amplification.

2.1.3 Procedure for making thin films with PLD

Preparation before deposition

1. Cut the substrate into a certain size. Anneal it if required.
2. Ultrasonically wash screws, clamps, and holders in acetone and ethanol, for five minutes for each.
3. Ultrasonically wash the substrate in acetone, ethanol, EL acetone, EL ethanol, five minutes for each.
4. Paste the substrate on the holder with flexible silver or platinum ink, and then fix it by screws and clamps.
5. Heat them on a hotplate, first at 100 °C for 30 minutes and then at 350 °C for 60 minutes.
6. Fix a target on the holder as well.

Operations inside the chamber

1. Stop a turbomolecular pump in the L/L chamber.
2. Place the substrate and the target on holders inside the chamber.

3. Evacuate the L/L chamber.
4. After sufficiently evacuating the chamber, transfer them inside the Main chamber.
5. Adjust the substrate temperature. Set the energy of the laser.
6. Introduce gas inside the chamber.
7. Ablate the target for five or ten minutes with the substrate covered by a mask.
8. Deposit the film.

After deposition

1. Cool down the substrate.
2. Stop introducing the gas.
3. Evacuate enough the chamber and the transfer the substrate.
4. Close a valve between the two chambers and then pick up the sample.
5. Carefully remove the substrate off the holder. All the parts should be polished well with a piece of sandpaper. Then they are ultrasonically washed in acetone and ethanol.

2.2 Topotactic reactions

2.2.1 Hydrogenation with calcium hydride

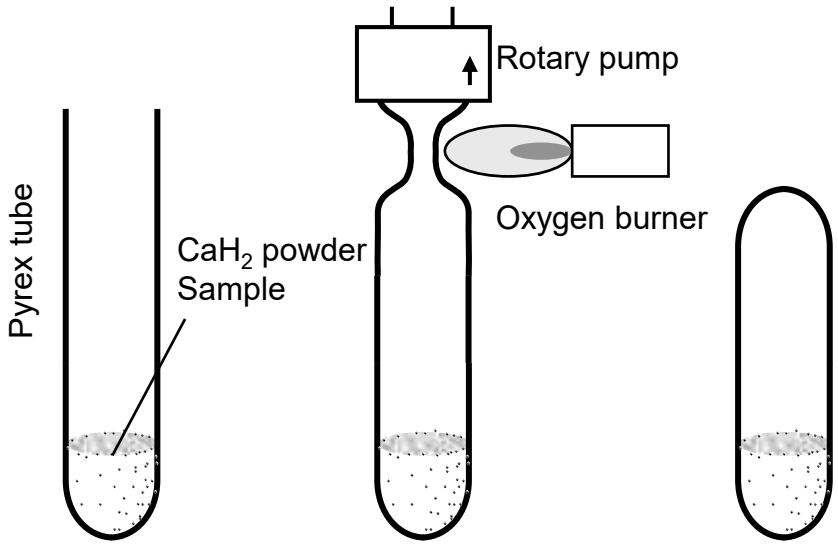

Figure 2-3. Vacuum sealing in a Pyrex tube.

In this study, calcium hydride (CaH_2) was used as a hydrogen source. As described in the introduction, CaH_2 can tolerate relatively high (ca. 600 °C) temperature. It is commercially available as pure powder, and it makes its handling easier than NaH, which is usually supplied as a mixture in mineral oil. Since CaH_2 vigorously reacts with moisture in air to decompose into CaO and H_2O, it should be kept in a glovebox filled with inert gas like Ar. The following procedure describes how to perform hydrogenation on a thin-film sample.

1. Cut a Pyrex tube to about 20 cm long.
2. Put a thin-film sample into the tube.
3. In a glovebox, grind CaH_2 powder for about five minutes.
4. Pour the ground powder into the tube.
5. Connect it to a rotary pump, and evacuate it for more than five minutes.

6. Seal it with a Bunsen burner (as in Figure 2-3).
7. Heat it in an electric furnace through an appropriate temperature sequence.
8. After the reaction, the tube is smashed to get the reacted film.
9. Reacted sample is ultrasonically washed in 2-butanone to remove residual powder on the surface of the film. The complete removal can be confirmed by XPS.

2.2.2 Fluorination with polyvinylidene fluoride (PVDF)

I used PVDF as a fluorination reagent because fluorination using PVDF is advantageous in that it is less likely to form metal fluoride impurities as discussed above. When PVDF is heated, thermal decomposition occurs. The products of this thermal decomposition cause the topotactic fluorination of oxide samples. As shown in Figure 2-4, the main product of the decomposition is a molecule with m/z = 20, i.e. HF, produced by the following reaction [54]:

$$[CH_2CF_2]_n \rightarrow [C{\equiv}C]_n + 2\ HF$$

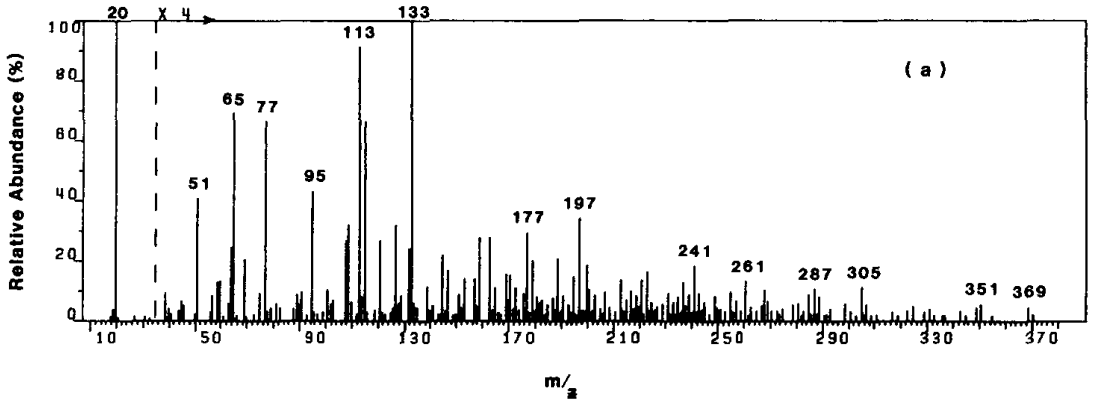

Figure 2-4. Mass spectrum from thermally decomposed PVDF at 470 °C. Reprinted from Ref [55], Copyright 1985, with permission from Elsevier.

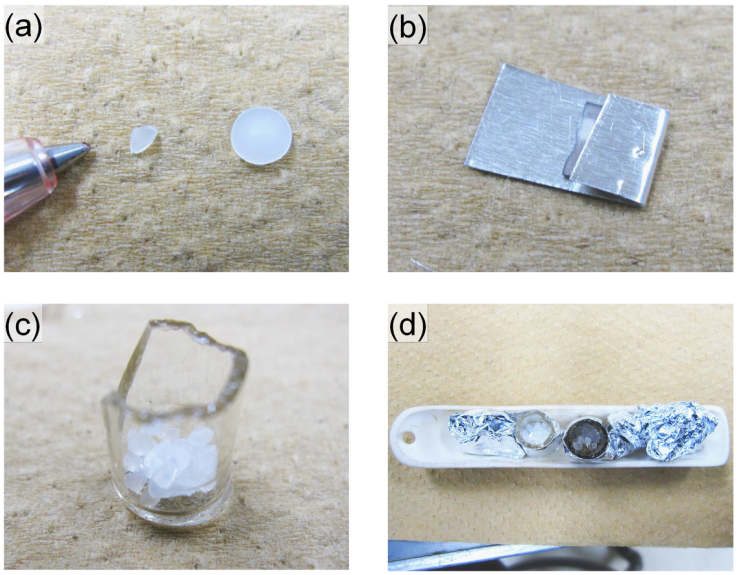

Figure 2-5. Photos of the fluorination process.

Figure 2-5 shows how to prepare the sample for fluorination. More detailed procedure is as follows:

1. As-purchased pellets (~ 4 mm diameter) were cut into eight pieces (a).
2. The thin-film sample was covered in a piece of aluminum foil to prevent direct contact between PVDF and the sample (b).
3. The sample and PVDF pellets were placed in a glass cup (c).
4. The cup with sample was set on an alumina boat (d).
5. The boat was placed in a tubular furnace, and heated under constant argon flow of 70 sccm. Excluding oxygen in the process would prevent oxidization and subsequent decomposition of the sample.

2.3 Evaluation of crystal structure by X-ray diffraction (XRD)

Discovered by von Laue in 1912, diffraction of X-rays is now widely used as a

fundamental tool for identifying the atomic structure of crystalline samples. In this section, the principles of XRD are briefly reviewed, and various scanning modes are introduced.

2.3.1 Principles

Bragg's law

When an X-ray with a certain wavelength λ is irradiated onto a crystalline specimen, it is reflected in discrete directions. Assuming that the specimen is made out of parallel planes spaced with a distance d, W. L. Bragg formulated the Bragg condition:

$$2d\sin\theta = n\lambda,$$

where n is a positive integer and θ is one half of the angle between the incident and reflected X-ray, i.e. the diffraction angle. Alternatively, the equivalent formula is obtained by introducing the notion of the reciprocal lattice. A reciprocal lattice is defined by three primitive vectors

$$\overrightarrow{b_1} = \frac{\overrightarrow{a_2} \times \overrightarrow{a_3}}{\overrightarrow{a_1} \cdot (\overrightarrow{a_2} \times \overrightarrow{a_3})},$$
$$\overrightarrow{b_2} = \frac{\overrightarrow{a_3} \times \overrightarrow{a_1}}{\overrightarrow{a_1} \cdot (\overrightarrow{a_2} \times \overrightarrow{a_3})},$$
$$\overrightarrow{b_3} = \frac{\overrightarrow{a_1} \times \overrightarrow{a_2}}{\overrightarrow{a_1} \cdot (\overrightarrow{a_2} \times \overrightarrow{a_3})},$$

where $\overrightarrow{a_1}, \overrightarrow{a_2}, \overrightarrow{a_3}$ are the three primitive vectors of a direct lattice. Using the notion of the reciprocal lattice, one can equivalently represent the condition for observing diffraction X-rays as

$$\Delta\vec{k} = h\overrightarrow{b_1} + k\overrightarrow{b_2} + l\overrightarrow{b_3},$$

where $\Delta\vec{k}$ is the difference between wave vectors of the incident and diffracted X-rays. This condition is called the Laue condition.

Optics of XRD

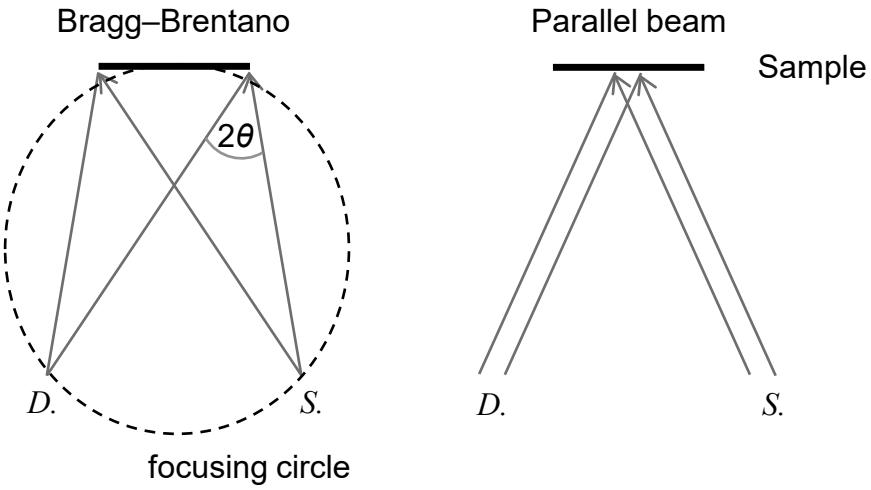

Figure 2-6. Two different optics in XRD. *S* and *D* represent the source of X-rays and the detector, respectively.

Figure 2-6 describes two typical optical set-ups used in XRD, which are referred to as Bragg–Brentano and parallel beam geometry. In Bragg–Brentano geometry, the X-ray source, the detector, and the sample are situated so that they form a focusing circle, on which the sample is tangentially positioned. Each diffracted X-ray with the same diffraction angle 2θ is parafocused onto the detector due to the inscribed angle theorem. This geometry is usually used for measuring powder samples because of its well-balanced sensitivity and precision as well as simplicity. To achieve perfect focusing, the sample has to be bent along the focusing circle, so measurements of flat samples have an inherent error.

On the other hand, to measure thin-film samples quantitatively, the parallel beam geometry is more suitable. In parallel beam geometry, the incident X-rays are collimated with a parabolically bent mirror made of a multilayer crystal (Göbel mirror). Parafocusing is no longer required, so one can choose the geometry of the sample with more degrees of freedom.

In this study, parallel beam geometry is used to evaluate the crystal structure of thin films as well as powder samples. Copper $K_{\alpha 1}$ radiation (λ = 1.5406 Å), monochromated through Ge double crystals, was adopted for most of the measurements. In 1D measurements of powder samples (described below) and all 2D measurements, Cu Kα1 and Kα2 rays were not separated; the averaged wavelength of them (1.5418 Å) was utilized for analyses.

2.3.2 Scanning modes

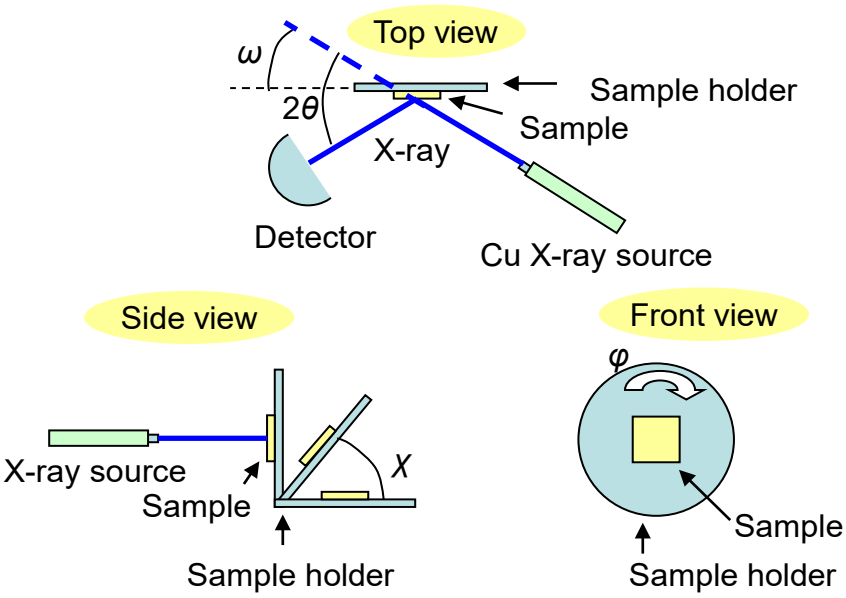

Figure 2-7. Geometry and drive parameters of the XRD system used in this study.

Figure 2-7 shows various positioning controllable in the present XRD system (Bruker D8 DISCOVER). When measuring oriented crystals such as epitaxial thin films, one must adjust these parameters so that the Laue condition is satisfied. For example, if out-of-plane diffractions, i.e. diffractions from lattice planes parallel to the substrate surface, χ must be set to be 90°. For detection of diffracted X-rays, I used three different kinds of detectors: 2D, 1D, and 0D (Figure 2-8). Each detector has its own advantages, as follows. The 2D detector can detect X-rays reflected out of the horizontal plane in

contrast to the other two, so one can get information about crystal orientation easily. The 0D detector has the highest resolution among the three. The resolution of the 1D detector is between that of 0D and 2D, but the diffraction intensity is high, so it is used to observe weak diffractions that are under the detection limits of the 0D or 2D detectors.

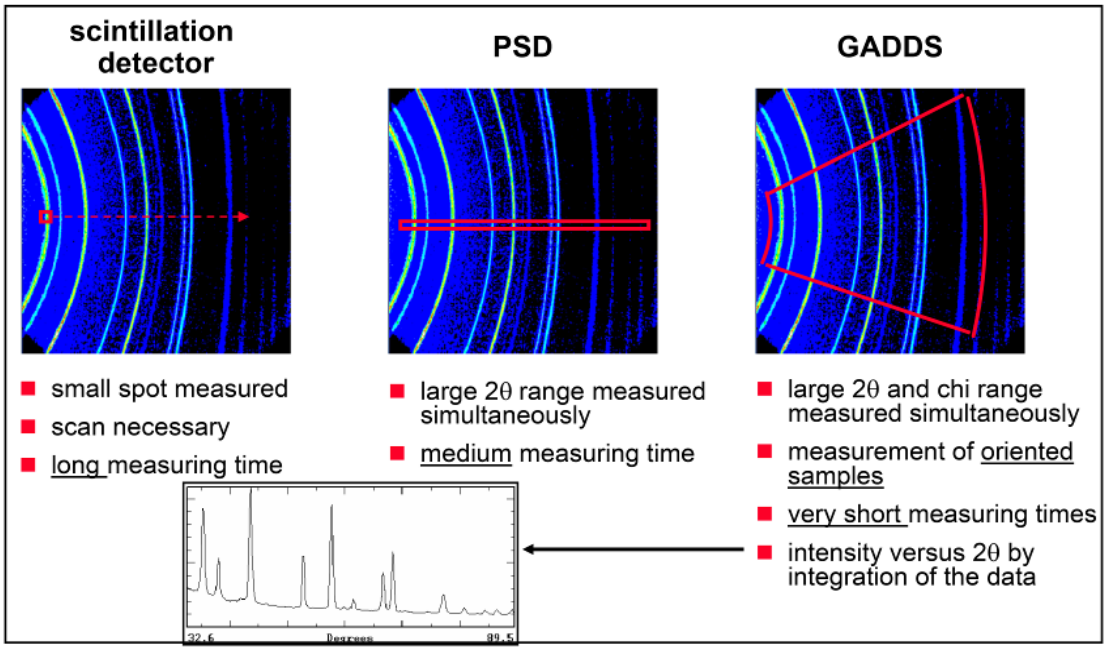

Figure 2-8. Comparison among 0D (scintillation detector), 1D (PSD), and 2D (GADDS) detectors Reproduced from Ref [56], Copyright 2000, JCPDS – International Centre for Diffraction Data (Open Access).

Several scanning modes are adopted to obtain various kinds of information about crystalline films. The following lists the operation and what kind of data can be obtained by each of them.

Locked coupled (2*θ*–*θ*) scan

In locked coupled or 2θ–θ scans, the sample angle ω is fixed to be one half of 2θ. Symmetric reflections from the substrate or the film are detected. When *c*-axis oriented epitaxial thin films are measured, with $\chi = 90°$, diffraction peaks appear at the positions of 00*l* (*l* =1, 2, 3…), from which the lattice parameter *c* is determined.

Rocking curve measurement (*ω* scan)

Rocking curves measurement is a useful way to evaluate the quality of thin films. In these measurements, the 2θ value is fixed at a certain diffraction that satisfies the Bragg's law, and intensity vs. ω plot is recorded. Roughly speaking, the full width half maximum (FWHM) of the peak in ω scan represents the degree of random deviation of crystalline lattice from complete alignment. Thus, the higher the crystallinity is, the smaller the FWHM becomes.

Reciprocal space mapping

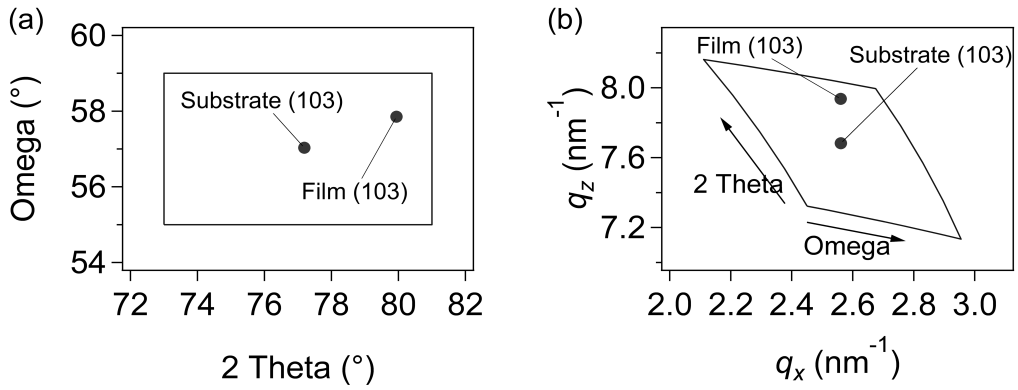

Figure 2-9. Conversion between real and reciprocal spaces in reciprocal space mapping measurements. Plot (a) shows scanning region in the direct space, while (b) shows that in the reciprocal space.

Reciprocal space mapping is a powerful method to visualize epitaxial relations between a substrate and film. In this measurement, a certain region in the reciprocal space is scanned by adjusting both 2θ and ω values. The parameters in the real space coordinate (2θ; ω) are converted into the reciprocal space coordination (q_x, q_z) by

$$q_x = \frac{1}{\lambda}(\cos(2\theta - \omega) - \cos\omega)$$

$$q_z = \frac{1}{\lambda}(\sin(2\theta - \omega) + \sin\omega),$$

where λ is the wavelength of the incident X-ray. An example of the conversion is depicted

in Figure 2-9. If the substrate and film have the same q_x value, the film is grown coherently, i.e. the in-plane lattice in the film are completely locked to that in the substrate.

2.4 Scanning transmission electron microscope (STEM)

Every quantum-mechanical particle has wave–particle duality. Just as electromagnetic waves show particle-like behaviors, electrons can act as wave with its wavelength of

$$\lambda = \frac{h}{p},$$

where h and p represent Planck's constant and the momentum, respectively. This property is the basis of electron microscopes which uses electron waves instead of electromagnetic waves. One of the advantages of electron microscopes originates from short wavelengths of electron waves. The wavelength of electrons accelerated through a voltage of 200 kV is as short as 2.5 pm, much smaller than that of visible rays (380–750 nm). Since the resolution of a microscope (Rayleigh's condition) is represented by

$$\delta = 0.61\frac{f\lambda}{a}$$

(a: radius of the aperture, f: the focal length of the lens), the shorter wavelength of electrons allows direct observation of atomic-level structure in a sample.

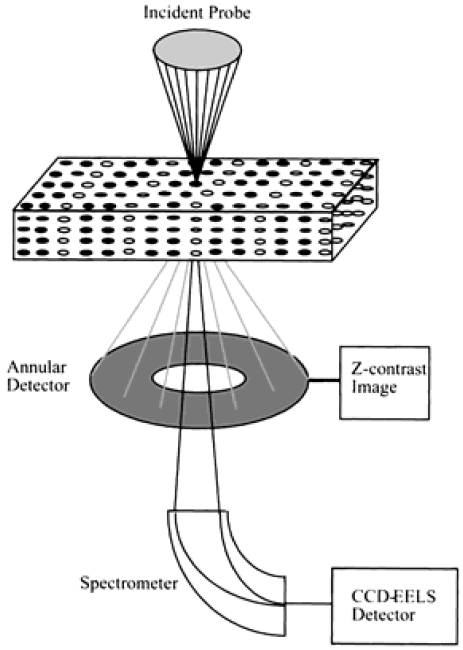

Figure 2-10 Schematic illustration of STEM. Reprinted from Ref [57] with permission from John Wiley and Sons, Copyright 2001.

Scanning transmission electron microscopy (STEM) is a member of transmission electron microscope (TEM) family. Figure 2-10 schematically illustrates the principles of STEM. In contrast to conventional TEMs that uses parallel incident electron beams, electron beams are focused onto the sample, and the sample is scanned to obtain an image. Transmitted electrons are categorized into two groups by their emergence angle. When electrons diffracted in lower angles (~ 10 mrad) are corrected, the image is called Bright-field (BF) image. The obtained image is rather similar to that obtained with a conventional TEM. On the other hand, if electrons emerging in higher angles (50–150 mrad) are collected, quite different images can be obtained. In these high-angle annular dark-field (HAADF) or *Z*-contrast images, interference effect among electron waves diffracted by different atoms is suppressed compared to BF images. As a result, the contrast of HAADF images is almost entirely determined by the atomic number Z at each point, while conventional TEM images contain crystallographic information as well. In this study, STEM is used to obtain complementary information about the atomic arrangement in the

samples.

2.5 X-ray photoelectron spectroscopy (XPS)

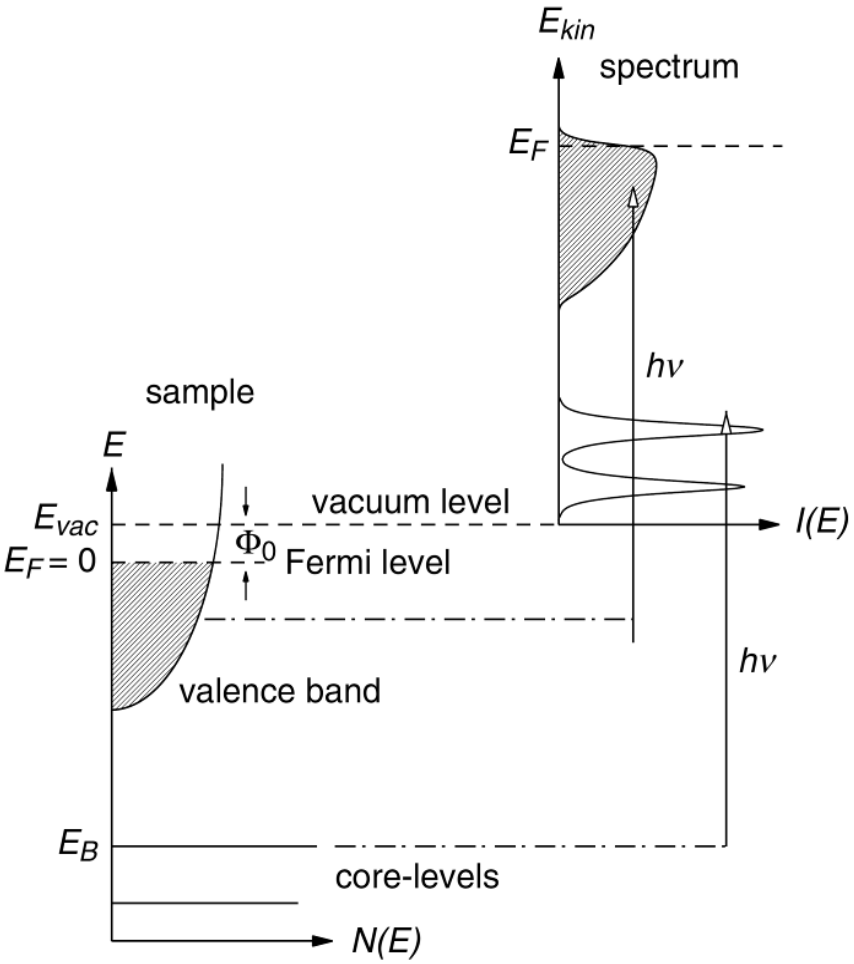

Figure 2-11 Schematic view of the photoemission process. E_B represents a binding energy of an electron. If the photon energy $h\nu$ satisfies $h\nu > E_B+\Phi_0$ (Φ_0: the work function of a sample), a photoelectron is emitted. Distribution of kinetic energies of photoelectrons correspond to the density of states in the sample material. Reprinted from Ref [58], licensed under CC BY-NC-SA version 3.0.

XPS is one of the most widely used techniques to obtain both qualitative and quantitative information about the atoms located near the surface of a sample. Figure 2-11

schematically describes the photoemission process. When ultraviolet or X-ray photons are irradiated on the surface to be analyzed, the energy $h\nu$ of a particular phonon is completely transferred into an electron in the sample with a binding energy E_B, which results in a photoelectron emission with kinetic energy

$$E_{kin} = h\nu - E_B - \Phi_0,$$

where Φ_0 is the work-function term of the order of several eV. Since the binding energy of a core-level electron is specific to each chemical element, constituent elements of the sample can be determined from the measured kinetic energy of photoelectrons. In addition, by observing slight change in E_B that reflects the chemical environment of an atom, it is possible to obtain chemical information such as chemical valence. Alternatively, by observing the intensity of photoelectrons emitted from the states near the Fermi level, one can obtain the information about the density of states (DOS) near the Fermi level. This helps us understand the physical properties of materials, because they are often governed by the nature of valence electrons.

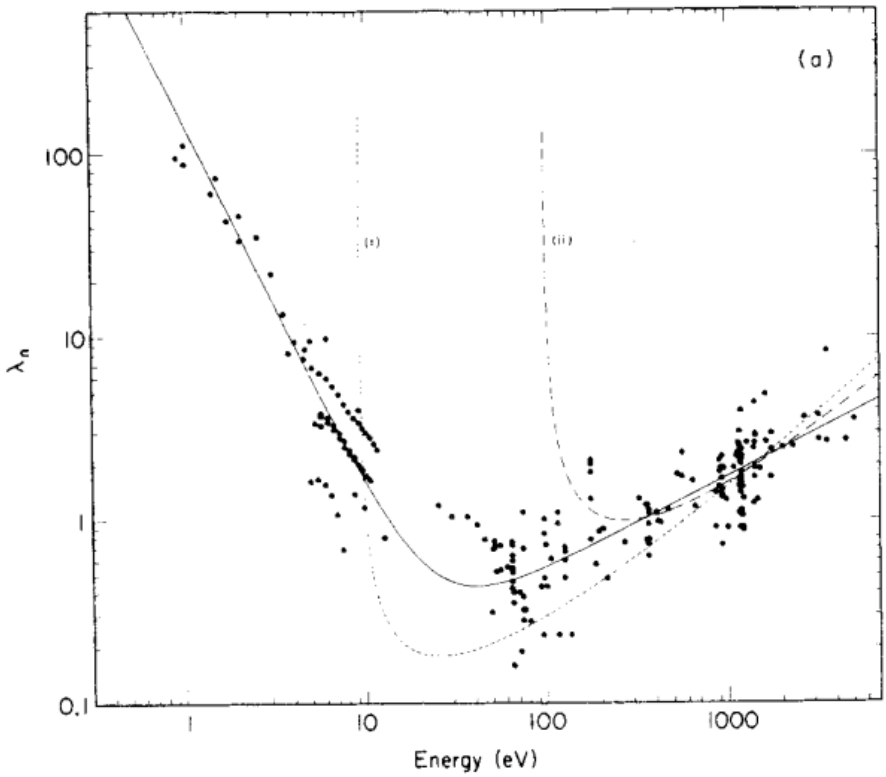

Figure 2-12. Inelastic mean free path (in nm) of electrons with different kinetic energies for various materials. Reprinted from Ref [59] with permission from John Wiley and Sons, Copyright 1979.

Electrons excited inside the sample need to travel a certain length through a solid matrix before losing their kinetic energies by inelastic collisions. This inelastic mean free path is a function of electron kinetic energy, and it represents the probing depth from the surface. As shown in Figure 2-12, at typical photon energies used for laboratory XPS (250–1500 eV), the mean free path is about 1–5 nm, which makes XPS surface sensitive. On the other hand, with higher energy X-ray photons or hard X-rays (up to 10 keV), the inelastic mean free path reaches the order of 10 nm, which enables more bulk-sensitive measurements. This technique is called hard X-ray photoelectron spectroscopy (HAXPES). Usually HAXPES is performed with synchrotron X-rays as light source, in order to make up for lower photoionization cross-sections of atoms against hard X-rays.

As mentioned before, the inelastic mean free path of photoelectrons are limited to

several nanometers. Therefore, to gain knowledges about the chemical composition in deeper regions, sputtering-assisted measurements are often required. In sputtering-assisted XPS, stepwise removal of the surface and measurements are performed by alternating cycles of sputtering and photoelectron measurements. In this study, I used ULVAC-PHI's PHI 5000 VersaProbe II available in Nano-Engineering Research Center, Institute of Engineering Innovation, School of Engineering, University of Tokyo. Aluminum Kα characteristic line ($h\nu$ = 1486.6 eV) was used as X-ray source. Depth profiling was performed with an Ar^+ sputtering gun with its acceleration voltage of 0.5–2 keV. XPS was employed to determine the relative difference in composition among samples. Quantitative composition analysis was done for a limited number of samples by using elastic recoil detection analysis, described in the next section.

2.6 Elastic recoil detection analysis (ERDA)

When the incident projectile beams with atomic number of Z_1, atomic mass of M_1, and kinetic energy of E_1 collide with target atoms, a process called Rutherford scattering occurs, which originates from Coulomb interaction between the two atoms. The kinetic energy of the recoiled atoms E_2 and that of the projectile E_S are expressed as

$$E_2 = \left(\frac{4M_1M_2}{(M_1+M_2)^2}\cos^2\theta\right)E_1,$$

$$E_S = \left[\frac{((M_2)^2-(M_1\sin\theta)^2)^{\frac{1}{2}}+M_1\cos\theta}{M_1+M_2}\right]^2 E_1,$$

where M_2 represents the atomic mass of recoiled atoms and θ the scattering angle. The recoil cross-section (in cm^2) for Rutherford scattering is:

$$\sigma_R = 5.18\times10^{-27}\left[\frac{Z_1Z_2(M_1+M_2)}{M_2E_1}\right]^2\frac{1}{\cos^3\theta},$$

with projectile energy E_1 given in MeV.

When measuring flat, solid samples, we can also obtain information about the depth

at which the scattering occurred by taking into account the energy loss before the recoiled atoms escape from the sample surface. Ions recoiled from a depth of x possesses the kinetic energy of

$$E' = E_2 - xN\varepsilon_R,$$

where N is the atomic density and ε_R is called *the recoil stopping cross-section factor*.

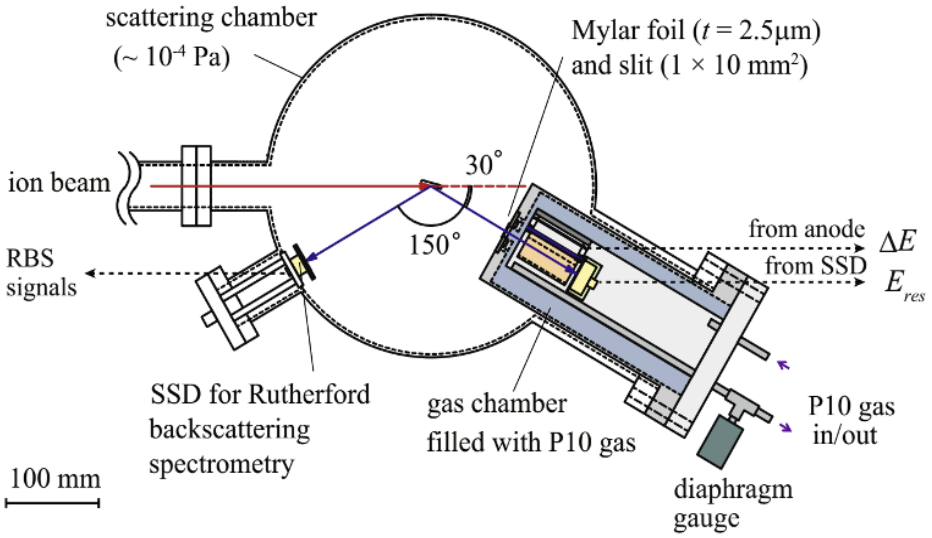

Figure 2-13. Schematic image of the ERDA system used in this study. Reprinted from Ref [60] with permission from Elsevier.

In Elastic Recoil Detection Analysis (ERDA), one observes the intensity of the recoiled target atoms (not the scattered projectiles) for quantitative evaluation of the amount of elements. The ERDA system used in this study is schematically shown in Figure 2-13. ERDA measurements were performed using a 38.4 MeV Cl^{7+} ion beam generated by the 5 MV tandem accelerator at Micro Analysis Laboratory, Tandem accelerator (MALT), University of Tokyo [60]. For chemical identification of elements, it is necessary to distinguish scattered elements with the same energy E' but with different atomic number Z_2. This can be achieved by the (ΔE – E) method, where the specific energy loss ΔE of the detected ions in a gas chamber was simultaneously observed along

with the kinetic energy E.

2.7 Energy-dispersive X-ray spectroscopy (EDS)

When an atom is ionized by electron beams, ion beams, or high-energy photons, the characteristic secondary X-ray is sometimes emitted. The wavelength of these characteristic X-rays is specific to each element, like binding energy of an inner-core electrons described in Section 2.5, which allows quantitative elemental analysis.

There are two methods to detect characteristic X-rays: wavelength-dispersive and energy-dispersive detections. In wavelength-dispersive detectors, emitted X-rays are dispersed using an analyzing crystal, which diffracts the X-ray beams based on the Bragg's law. Though this method has high energy resolution, the experimental setups tend to be rather complex. In the other method, energy-dispersive detection, the beams are introduced in a semiconductor detector that generates electron-hole pairs by X-ray excitation. By counting the number of generated electron-hole pairs, the energy of emitted photons can be estimated.

In this study, an EDS system equipped in a scanning electron microscope (JEOL JSM-7100F) was used. Its energy resolution was 130 eV.

2.8 Secondary ion mass spectrometry (SIMS)

SIMS is one of ion beam sputtering technique. First, primary ions accelerated at several keVs are irradiated on the specimen. When an enough amount of the kinetic energy of the primary ions is transferred on an atom in the specimen, it is sputtered out of the sample surface. While more than 90 % of the sputtered species are charge-neutrals, a small amount of them are released as charged particles. These secondary ions were analyzed by mass spectrometry to obtain quantitative information. An important

advantage of this method is that it can detect all elements, from hydrogen to uranium. Furthermore, it can distinguish different isotopes, e.g. ^{1}H and ^{2}D, and has extremely low detection limits (~ 100 ppt). A potential drawback is significant matrix effect resulting from complicated relations between measured secondary-signals and the chemical composition of the sample.

In this thesis work, SIMS was used to investigate concentration of hydrogen inside samples. Primary ions were Cs^{+} with acceleration voltage of 1.0 keV. To perform quantitative analysis, $SrTiO_3$ with a known amount of implanted hydrogen was used as reference for all measurements.

Chapter 3. Synthesis of defect-fluorite $NdNiO_xH_y$ from $NdNiO_3$ precursors: growth and crystal orientations*

3.1 Introduction

The topotactic reaction of transition-metal oxides with metal hydrides is utilized as a facile and efficient synthesis approach for novel or mixed-anion oxides [61,62]. In this class of reaction, metal hydrides can act as either strong reducing reagents for removing oxide anions or incorporating hydride anions. Reactions with the former role yield transition-metal oxide phases with exceptionally low oxidization states (Ni^+, Ru^{2+}, Co^+) [6,63–66], unusual coordination networks (square-planar Fe^{2+}) [27], or both, while those with the latter allow the preparation of oxyhydrides [29,33,35] such as $LaSrCoO_3H_{0.7}$, $BaTiO_{3-x}H_x$, and $SrVO_2H$. Topotactic reactions can be performed at low reaction temperatures; for example, a typical reaction temperature during oxygen deintercalation or hydride ion incorporation is below 500 °C, which is considerably lower than those of conventional "hard" solid-state reactions (~1000 °C). Reactions at these low temperatures, classified as "soft" chemical reactions, enable the synthesis of metastable compounds, such as oxyhydrides, that can decompose easily at elevated temperature.

Although topotactic reactions are typically used to produce powdered samples, several groups have applied the metal-hydride reaction to thin films, reporting fabrications of $LaNiO_2$ [47,48], $SrFeO_2$ [67], $Sr_{1-x}Eu_xFeO_2$ [68], $ATiO_{3-x}H_x$ [69] (A = Ca,

---

* This chapter contains the contents of the following publication.

"Formation of defect-fluorite structured $NdNiO_xH_y$ epitaxial thin films via a soft chemical route from $NdNiO_3$ precursors,"
Tomoya Onozuka, Akira Chikamatsu , Tsukasa Katayama, Tomoteru Fukumura, and Tetsuya Hasegawa,
Dalton Transactions, **30**, 12114 (2016),

Ba, or Sr), $SrCoO_xH_y$ [36], and $LaSrCoO_{4-x}H_x$ [51] as thin films. The topotactic reaction of epitaxial thin films allows the preparation of single-crystalline films, which can be used to measure the intrinsic physical properties of materials. In addition, the concentration of introduced heteroatoms can be much higher in films than in bulk samples because of the higher reactivity of thin films. Katayama *et al.* [70] recently reported that a $SrFeO_2$ thin film, obtained by a topotactic reaction between $SrFeO_{2.5}$ and CaH_2, contained a significant amount of hydrogen (~3×10^{21} atoms/cm^3). The hydrogen could serve as an electron acceptor and generate metallic conductivity, in contrast with bulk $SrFeO_2$.

Here, I investigate the topotactic reaction of perovskite $NdNiO_3$ epitaxial thin films with CaH_2. Perovskite $NdNiO_3$ shows a metal–insulator transition at 200 K [1] associated with charge ordering and a structural transition [71]. The reduction of $NdNiO_3$ powder using metal hydride was reported to yield infinite-layer $NdNiO_{2+x}$ [6,63], although the presence of hydrogen in the reduced product was not confirmed. In this study, I found that the CaH_2 treatment of $NdNiO_3$ epitaxial thin films completely altered the cation framework, producing defect-fluorite-structured $NdNiO_xH_y$. Moreover, the growth orientation of the defect-fluorite phase changed as a function of the reaction temperature with CaH_2.

3.2 Experimental methods

Epitaxial $NdNiO_3$ thin films were deposited as precursors onto $SrTiO_3$ (STO) (100) substrates (Shinkosha Co., Ltd.) by pulsed laser deposition (PLD) at a substrate temperature of 650 °C, oxygen partial pressure of 13 Pa, laser (KrF excimer, 248-nm wavelength) fluence of 2 J/cm^2, and repetition rate of 5 Hz. The obtained precursor films were then reacted with CaH_2 powder (Wako Pure Chemical Industries, Ltd.) in a Pyrex tube evacuated with a rotary pump. The reaction temperature and reaction time were varied in the ranges of 240–400 °C and 1–24 h, respectively. After the reaction, the film

was ultrasonically washed with 2-butanone to remove residual powders from the surface. The crystal structures of the samples were characterized by X-ray diffraction (XRD, Bruker AXS D8 Discover) with Cu Kα radiation, as well as by high-angle annular dark-field scanning transmission electron microscopy (HAADF-STEM, Hitachi High-Technologies Co., HD-2700). The amount of hydrogen within the films was measured by dynamic secondary-ion mass spectrometry (SIMS, ULVAC-PHI PHI-ADEPT1010, primary ion: Cs^+, secondary ion: H^-, acceleration voltage: 1.0 kV, detection limit: 1×10^{19} cm^{-3}, depth resolution: ~3 nm).

3.3 Results and Discussion

Figure 3-1 shows out-of-plane 2θ–θ XRD patterns of the precursor $NdNiO_3$ film on the STO (100) substrate and the film after reaction with CaH_2 at 240 °C for 12 h. The pattern of the precursor films shows the 002 diffraction peak of perovskite $NdNiO_3$ at 2θ = 48.05°. The out-of-plane lattice constant *c* is calculated as 3.78 Å, in good agreement with previously reported values [72,73]. Reciprocal space mapping (RSM) around the 103 asymmetric diffraction (Figure 3-2b) reveals that the in-plane lattice of the $NdNiO_3$ (*a*-axis) is completely locked to the STO substrate. The in-plane lattice constant is larger than the out-of-plane one, indicating that the film is under in-plane tensile strain from the substrate. Meanwhile, in the 2θ–θ pattern of the film treated with CaH_2 (Figure 3-1a), the peak from $NdNiO_3$ has completely disappeared; a new peak at $2\theta \approx 55.8°$ (d = 1.65 Å) has emerged, which corresponds to the 002 diffraction of infinite-layer $NdNiO_2$. In RSM (Figure 1c), the $NdNiO_2$ 103 peak is located just above that of STO 103, demonstrating that the epitaxial relation between film and substrate is maintained during the chemical reaction with CaH_2. However, the intensity of the $NdNiO_2$ 002 diffraction is much weaker than that in the pattern of the precursor film. Furthermore, in the RSM image, the diffraction spot is significantly elongated along the q_z direction. These changes suggest

that $NdNiO_2$ exists as a very thin layer within the film.

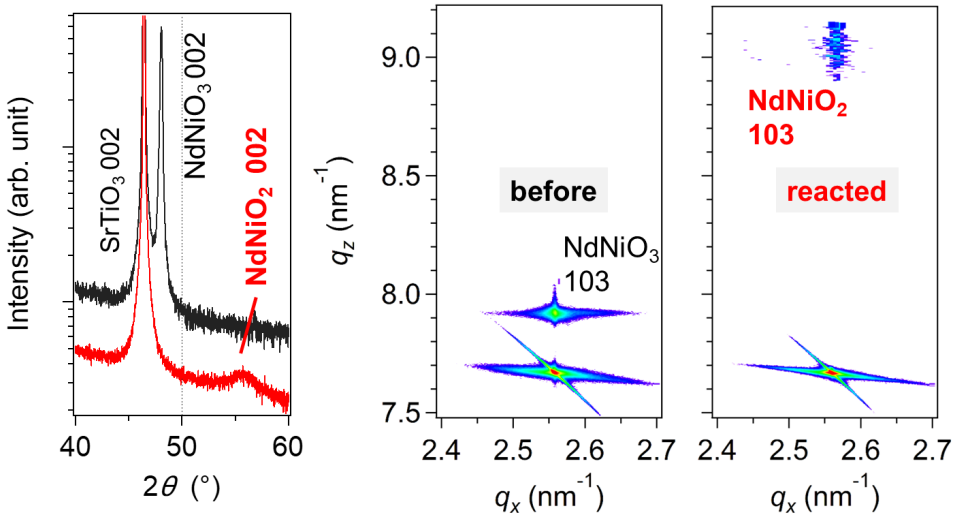

Figure 3-1. (a) XRD 2θ–θ patterns before (black) and after (red) the reaction with CaH_2 at 240 °C. Reciprocal space maps (b) before and (c) after the reaction.

To obtain further information on the crystal structure, I performed atomic-level HAADF-STEM imaging of the CaH_2-treated film. Figure 3-2a shows a large area (~200 nm width) HAADF image of the CaH_2-treated film, indicating almost no contrast. Since the brightness of HAADF images depends on the atomic number of the constituent elements, the lack of contrast indicates that neodymium and nickel are homogeneously distributed in the film with no cation segregation. Figure 3-2b is a high-resolution image taken near a film/substrate interface. In the region near the substrate (Region ii), a rectangular lattice with (a, c) = (3.9 Å, 3.3 Å), representing c-axis oriented $NdNiO_2$, is observed. The thickness of this region is approximately ten monolayers; this explains the weakness and breadth of the $NdNiO_2$ diffraction peak in Figure 3-1. Figure 3-2b also indicates the presence of a thin interfacial layer measuring ~0.5 nm in thickness (Region i). A similar interfacial layer was observed in infinite-layer $Sr_{0.9}La_{0.1}CuO_2$ thin films grown by molecular-beam epitaxy [74]; it was proposed to promote the growth of the

infinite-layer phase.

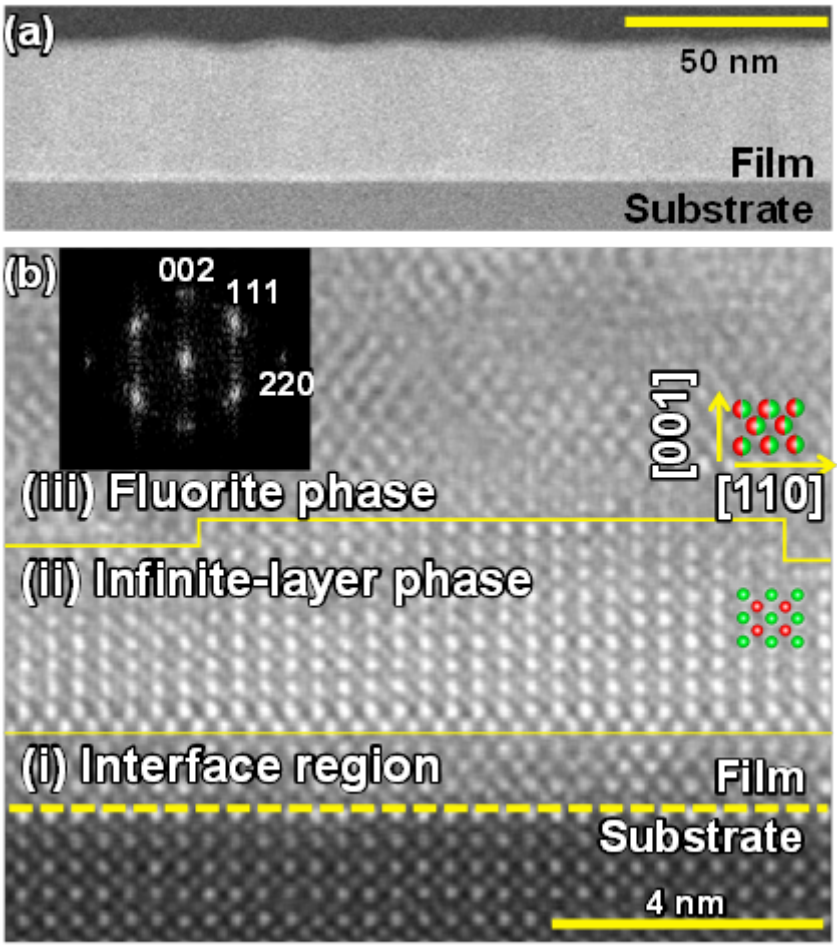

Figure 3-2. (a) Wide and (b) magnified view of HAADF-STEM images after the reaction at 240 °C for 12 h. Inset: Fourier transform of the fluorite phase region (iii). Green and red circles show the positions of neodymium and nickel atoms, respectively.

Meanwhile, the atomic arrangement in Region iii, located above Region ii and occupying most of the film, is completely different from that of $NdNiO_2$: each atom in Region iii is imaged with a contrast brighter than that of nickel but darker than that of neodymium in Region ii. This suggests that the metals are randomly distributed in Region iii. The lattice image in Region iii can be understood by assuming a face-centered cubic (fcc) lattice viewed along the [110] direction, as depicted by the green and red points in

the figure. From the Fourier transform of the HAADF image (inset in Figure 2b), the lattice constant is estimated as 5.5 Å. The observed atomic arrangement and lattice constant are near those of a fluorite-structured oxyhydride, NdHO (a = 5.61 Å in pseudocubic notation) [75]. Therefore, I tentatively conclude that the reaction of $NdNiO_3$ with CaH_2 yields a fluorite-structured NdHO-related phase as a major component of the film; hereafter, this is called the fluorite phase.

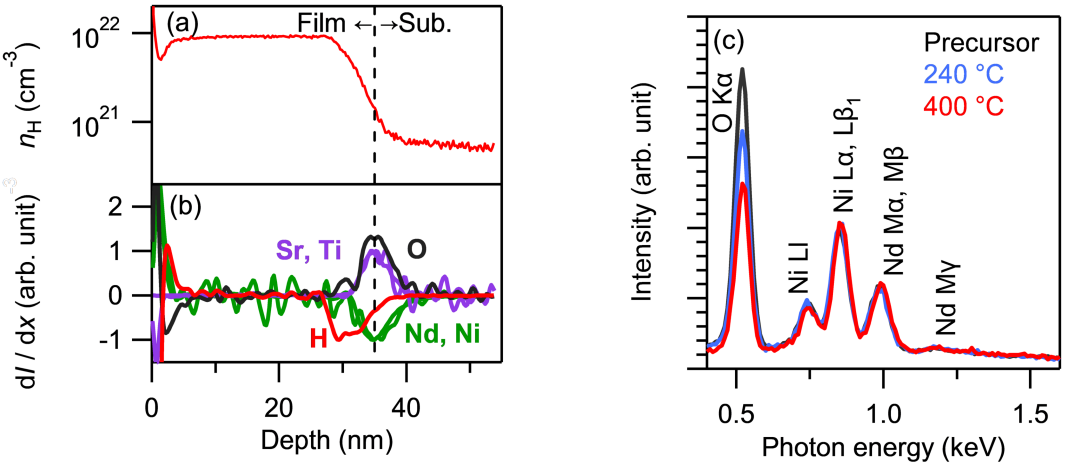

Figure 3-3. (a) Depth dependence of atomic hydrogen density (n_H) after the reaction at 240 °C. (b) Differential secondary-ion intensity (dI/dx) of each element. (c) EDS spectra of the films before (black) and after the reaction (blue, red), measured at an acceleration voltage of 2.5 kV.

In order to determine the chemical composition of this NdHO-related fluorite film, I performed dynamic SIMS and EDS measurements. Figure 3-3a shows a hydrogen depth profile measured by SIMS for the sample treated with CaH_2 at 240 °C, clearly indicating that hydrogen is homogeneously distributed in the film. The hydrogen density is evaluated as ~9 × 10^{21} atoms/cm^3 (0.7 per formula unit, fu), although this has some uncertainty because hydrogen-implanted STO was used as a standard reference. The hydrogen density in the substrate was more than one order of magnitude smaller than that in the film. Figure 3b plots the differential secondary-ion intensities of strontium, titanium,

neodymium, nickel, and hydrogen. As observed, the hydrogen density abruptly drops at a position several nanometers shallower than the film–substrate interface. This indicates that hydrogen is mainly incorporated into the fluorite phase, rather than the infinite-layer $NdNiO_2$.

Figure 3-3c compares the EDS spectra of the film before and after the reaction with CaH_2. The nickel/neodymium ratio remains constant, whereas the intensity of the O Kα peak is suppressed by 20% after the reaction. Assuming that the peak intensity of each element is proportional to its concentration, the oxygen density is estimated as 2.3/fu. From these results, the chemical formula of the fluorite phase is estimated as $NdNiO_xH_y$ with $(x, y) \approx (2.3, 0.7)$. The total anion (oxygen + hydrogen)/cation (neodymium + nickel) ratio is approximately 3/2, smaller than the ideal value of 2, which suggests that the obtained oxyhydride phase has the defect-fluorite structure.

Finally, I describe the selective synthesis of the oxyhydride phase via solid-phase reaction with CaH_2 at higher temperature. Figure 3-4a and 4b show the out-of-plane (χ = 90°) and asymmetric (χ = 35°) XRD patterns for the film prepared at 400 °C. Notably, the former indicates no peaks assignable to the infinite-layer $NdNiO_2$ phase, whereas a clear peak from the fluorite oxyhydride phase is observed in the latter, demonstrating the formation of a phase-pure oxyhydride phase without infinite-layer $NdNiO_2$. The peak at 2θ = 28° in Figure 3-4b is assignable to the 111 diffraction of the fluorite phase. This implies the oxyhydride film heat-treated at 400 °C is [110]-oriented, in contrast to the film prepared at 240 °C with [001]-orientation. A HAADF-STEM measurement also confirms this orientation change. Most of the film consisted of the [110]-oriented crystals (as in Figure 3-4c), while the crystals adjacent to the substrate–film interface (2–3 nm thick, Figure 3-4d) remained [001]-oriented. Additionally, SIMS measurement revealed that this sample contained 6×10^{21} cm^{-3} of hydrogen (0.5/fu), comparable to that of the sample prepared at the lower temperature of 240 °C (0.7/fu). The EDS measurement

confirmed that the neodymium and nickel contents in this film were invariant after the heat-treatment, while the oxygen content decreased from 2.3 (at 240 °C) to 1.7 (at 400 °C). If hydrogen is present as H^-, H, or H^+, the nominal valence state of nickel is calculated to be +0.9, +0.4, or −0.1, respectively. Though +3 (as in $NdNiO_3$), +2 (as in NiO), and +1 (as in $NdNiO_2$) states of nickel are known in extended oxides, to the best of our knowledge, there are no reports on zero or negative charge states of nickel oxides. Therefore, it seems natural to assume that hydrogen exists as hydride anions rather than protons or charge-neutral atoms.

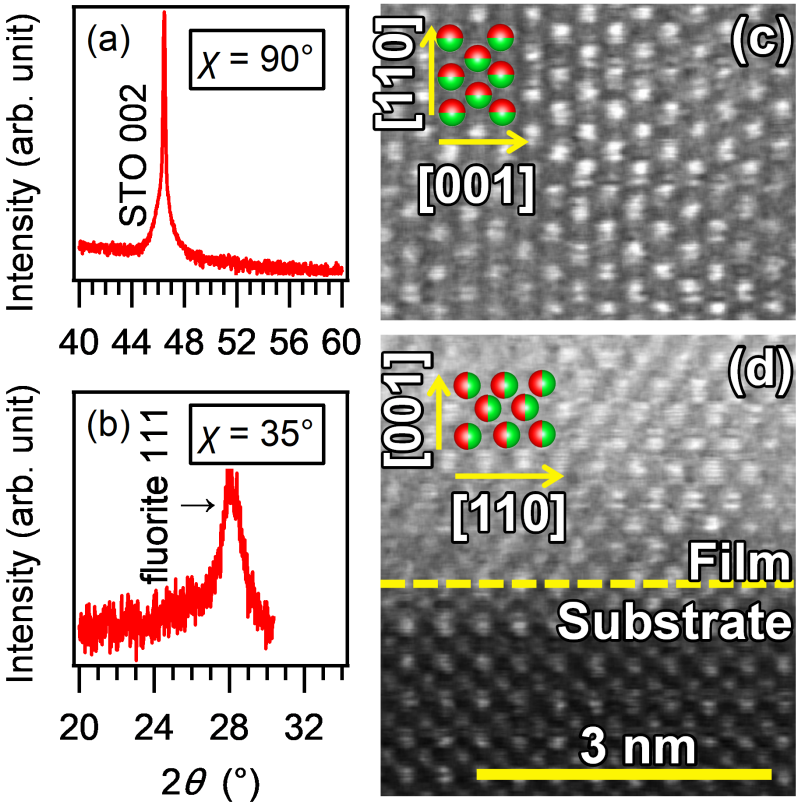

Figure 3-4. (a) Out-of-plane ($\chi = 90°$) and (b) in-plane ($\chi = 35°$) XRD patterns of the films reacted at 400 °C for 24 h. HAADF-STEM images of the film reacted at 400 °C for 24 h (c) at the middle of the film and (d) at the interface between the film and the substrate.

In the [001]-oriented fluorite film obtained at 240 °C, the [110] and [1-10] axes of

$NdNiO_xH_y$ are parallel to the [100] and [010] directions of the STO substrate, respectively. The cubic lattice constant a of the substrate (3.905 Å) and $a/\sqrt{2}$ of the fluorite phase (≈ 3.9 Å) are nearly equal; thus, it is natural that [001]-orientated fluorite is grown on STO (100). Meanwhile, the orientation change mentioned above is contrary to my prediction based on the epitaxial relation between the fluorite film and substrate. In the [110]-oriented $NdNiO_xH_y$ film obtained at 400 °C, the [1-10] and [001] axes are parallel to the [100] and [010] directions of the substrate, respectively. In this orientation, the in-plane lattice of $NdNiO_xH_y$ has a rectangular shape with axes of 3.9 Å (along $[100]_{substrate}$) and 5.5 Å (along $[010]_{substrate}$). The latter value is incommensurable with that of the substrate and thus the [110]-oriented $NdNiO_xH_y$ film is expected to have a lattice match poorer than that of the [001]-oriented crystal. A similar orientation change was reported in $LaNiO_2$ thin films obtained by the topotactic reduction of $LaNiO_3$, in which c-axis-orientated $LaNiO_2$ with better lattice matching transformed to a-axis-orientated $LaNiO_2$ with poorer lattice matching as the reaction time or temperature increased [76].

These results suggest that the crystal growth direction is determined by kinetics rather than by thermodynamics including epitaxial stabilization. One possible explanation is that the anisotropic diffusion of atoms promotes a specific arrangement of atoms with respect to the substrate lattice. Because the topotactic reaction on thin films mainly occurs from their surfaces, the atomic diffusion perpendicular to the film surface dominates the reaction [77]. The growth of (110) oriented $NdNiO_xH_y$, contrary to my expectation, may be the consequence of such perpendicular diffusion of the constituting atoms. Further studies on chemical transport properties such as anisotropic ionic conductivity may help to elucidate the detailed mechanisms.

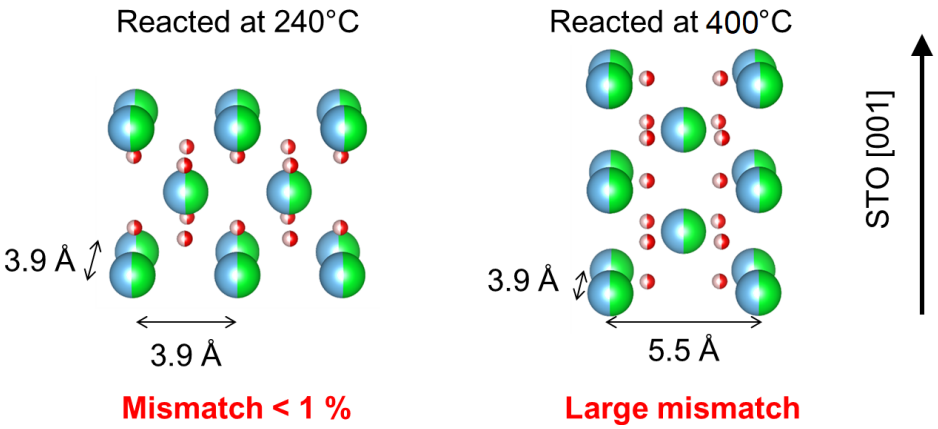

Figure 3-5. Comparison of crystal orientations of the oxyhydride $NdNiO_xH_y$ films reacted at different temperatures.

3.4 Conclusions

I have investigated the soft chemical reaction of $NdNiO_3$ thin films with CaH_2. As seen in Figure 3-5, when the precursor film was reacted at 240 °C, [001]-oriented $NdNiO_xH_y$ ($x \sim 2.3$, $y \sim 0.7$) with a defect-fluorite structure was grown on a thin interfacial layer of infinite-layer $NdNiO_2$. At the elevated reaction temperature of 400 °C, I observed the growth of a [110]-oriented defect-fluorite phase, although it seemed more poorly lattice-matched to $SrTiO_3$ [100] than the [001]-oriented $NdNiO_xH_y$ did.

The incorporation of a large amount of hydrogen into the films suggests the potential of $NdNiO_x$ for hydrogen storage. Hydrogen storage using single crystals is not practical because of small surface/volume ratio. However, they are useful for the observation of fundamental kinetics of diffusion-controlled reactions.

Chapter 4. Topotactic synthesis of $NdNiO_{3-x}F_x$ thin films and their electrical properties[†]

4.1 Introduction

Transition-metal oxides exhibit a wide variety of electronic and magnetic properties owing to the interplay between the multiple degrees of freedom, such as the charge, lattice, spin, and orbital [1,78]. These properties include multiferroicity [79], the Mott transition [80], and high-*T*c superconductivity [81]. Among these materials, rare-earth nickelates ($RNiO_3$, where *R* represents rare earth elements) have been the subject of long-standing interest in the nascent field of oxide electronics. $RNiO_3$ is known to undergo a first-order metal-insulator transition (MIT), depending on the ionic radius of R [82,83]. While the detailed mechanism of the MIT is still a matter of debate, it has been suggested that the charge disproportionation of nickel ions ($Ni^{3+} \rightarrow Ni^{(3+\delta)+}$ / $Ni^{(3-\delta)+}$) plays a crucial role in the MIT [71,84–87]. The resistance change of one to two orders of magnitude that is associated with the transition has been exploited to develop electronic devices called Mott transistors. Among the various $RNiO_3$ materials being explored, $NdNiO_3$, which exhibits a temperature-driven MIT at ~200 K, is among the most widely studied nickelates. It has been reported that the transition temperature of $NdNiO_3$ can be lowered by gating with an electric double-layer transistor; the application of a negative gate voltage decreased TMI by ~40 K [88,89]. However, to be able to electrically control

---

[†] This chapter contains the contents of the following publication.

"Reversible Changes in Resistance of Perovskite Nickelate $NdNiO_3$ Thin Films Induced by Fluorine Substitution,"
Tomoya Onozuka, Akira Chikamatsu , Tsukasa Katayama, Yasushi Hirose, Isao Harayama, Daiichiro Sekiba, Eiji Ikenaga, Makoto Minohara, Hiroshi Kumigashira, and Tetsuya Hasegawa,
ACS Applied Materials & Interfaces, **9**, 10882 (2017),

the phase transition in $NdNiO_3$, an ultrathin film with thickness of less than 10 nm is required because a large amount of carriers are present in the metallic state (~10^{22} cm^{-3}).

Chemical modification is an alternative approach for modulating the resistance of this material. A typical example is aliovalent substitution at the Nd site in $NdNiO_3$; the substitution of either divalent (Sr^{2+} or Ca^{2+}) or tetravalent (Th^{4+}) ions for Nd^{3+} produces hole or electron carriers, respectively, and subsequently lowers the transition temperature [90]. Recently, proton doping at the interstitial sites and the incorporation of oxygen vacancies have also been attracted much attention, because the related chemical reactions, namely, the incorporation/extraction of hydrogen or oxygen, is often reversible, potentially allowing for the reversible switching of the resistance. Ramanathan and co-workers doped protons into $RNiO_3$ (R = La, Nd, Sm, or Eu) using a platinum-catalyzed intercalation reaction [91,92] while Wang et al. introduced oxygen vacancies into $NdNiO_3$ through annealing in a vacuum [93]. In both cases, an increase in resistance by more than six orders of magnitude was observed.

The aliovalent substitution of fluoride ions at the oxygen sites would also provide additional electrons to the nickel ions and significantly change the electronic properties of perovskite nickelates. Furthermore, the fluorine substituted at the oxygen sites would directly affect the connectivity of the Ni-anion network, which is responsible for electrical conduction in the nickelates. Thus, fluorine substitution may have as large effect on the electric conductivity as proton or oxygen-vacancy doping. Here I demonstrated fluorine substitution in epitaxial $NdNiO_3$ thin films through low-temperature topotactic fluorination with polyvinylidene fluoride (PVDF) [45,49,94] and investigated the physical properties as well as the electronic structures of the doped thin films. After fluorine incorporation, the films showed highly insulating properties, with the room-temperature resistivity being more than six orders of magnitude higher than that of as-grown $NdNiO_3$. Soft X-ray absorption and hard X-ray photoelectron and spectroscopies

(XAS and HAXPES, respectively) revealed that the chemical valence of the Ni ions changed from Ni^{3+} to Ni^{2+} with the fluorine substitution In addition, the electronic density of states at the Fermi level (E_F) decreased. Moreover, the incorporated fluorine could be removed completely by annealing the thin films in oxygen, leading to conclusion that it should be possible to fabricate resistance-switching devices by controlling the fluorine content in $NdNi(O,F)_3$.

4.2 Experimental Methods

Epitaxial $NdNiO_3$ thin films with a thickness of ~70 nm were deposited as precursors onto $SrTiO_3$ (100) (STO) substrates (Shinkosha Co., Ltd.) by pulsed laser deposition. The deposition conditions were as follows: substrate temperature of 650 °C, oxygen partial pressure of 13 Pa, laser (KrF excimer, 248-nm wavelength) fluence of 2.0 J cm^{-2}, and repetition rate of 5 Hz. The fabricated precursor films were then reacted with polyvinylidene fluoride (PVDF) pellets (Fluorochem Ltd.) to introduce fluorine. The precursor film was heated with 0.1 g of PVDF in an argon gas flow of 70.0 mL min^{-1}. In keeping with the method previously developed by our group, the film was tightly wrapped in Al foil, and PVDF pellets were placed on the foil. Wrapping was used in order to prevent the adhesion of the charcoal-like residue produced by the decomposition of PVDF [49]. The reaction temperature and time were varied between 240–350 °C and 3–24 h, respectively.

The crystal structures of the films were characterized by X-ray diffraction (XRD) analysis (Bruker AXS D8 Discover) performed using Cu-Kα radiation. The film thicknesses were measured by the X-ray reflectivity method (Bruker AXS D8 DISCOVER). The chemical compositions of the films were measured using X-ray photoelectron spectroscopy (XPS, ULVAC-PHI PHI5000 VersaProbe), which was performed using an Al-Kα X-ray source and Ar^+ sputtering; scanning electron

microscopy-energy dispersive X-ray spectroscopy (SEM-EDS, JEOL JSM-7100F); and elastic recoil detection analysis (ERDA), which was performed using a 38.4 MeV Cl7+ ion beam generated by the 5 MV tandem accelerator at Micro Analysis Laboratory, Tandem accelerator (MALT), the University of Tokyo [60]. The optical gap values were determined using an UV–visible–near-infrared (UV–Vis–NIR) spectrometer (Jasco V670DS). The HAXPES spectra of the core levels and valence bands were measured with an electron energy analyzer (VG SCIENTA Scienta R-4000), which had an energy resolution of 0.27 eV, at a photon energy of 7.94 keV at beamline BL47XU at the SPring-8 facility. The XAS spectra were measured by the total-electron yield method using beamline BL-2A at the Photon Factory, KEK. All the spectra were measured at 300 K. Finally, the electrical resistivities of the samples were measured in a cryostat (Quantum Design PPMS) using the four-wire geometry.

4.3 Results and Discussion

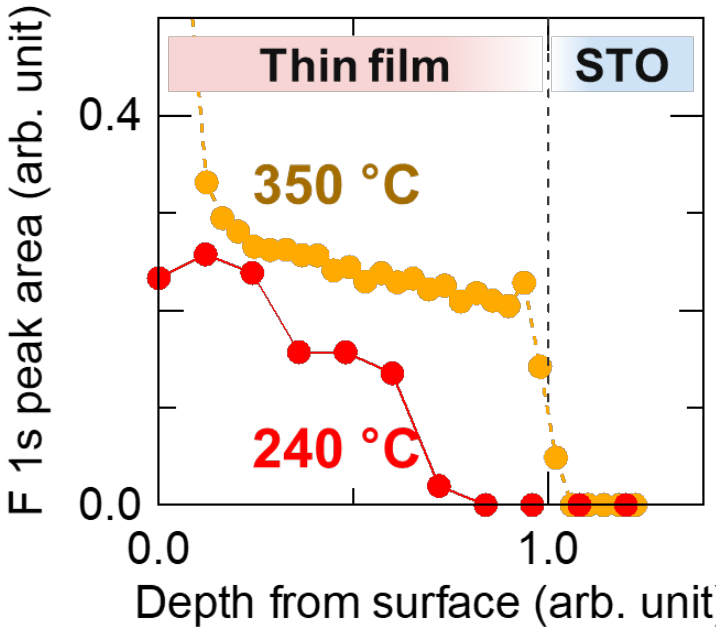

Figure 4-1. Depth profile of fluorine inside the film after reaction with PVDF, measured by sputter-assisted XPS.

First of all, I optimized the reaction temperature during reaction with PVDF. Figure 4-1 shows fluorine concentration depth profile measured by sputter-assisted XPS. There are two plots from different samples; one is reacted at 350 °C and the other at lower temperature of 240 degrees. Reaction time was same: 12 hours for both samples. At 350 degrees, the entire depth region of the thin film was fluorinated. In contrast, when $NdNiO_3$ and PVDF were reacted at 240 °C, fluorine distribution was quite inhomogeneous and the deeper region of the film was not fluorinated. This could be interpreted by considering reaction mechanisms. In topotactic reaction, two kinetic factors are important: ion exchange at surface, and inner diffusion of oxygen and fluorine atoms. If the temperature is too low, poor diffusion prevents preparation of homogeneous samples. Thus, moderately high temperature of 350 °C was required for enough inner diffusion of fluorine. In the following discussion, the reaction temperature was fixed at 350 °C.

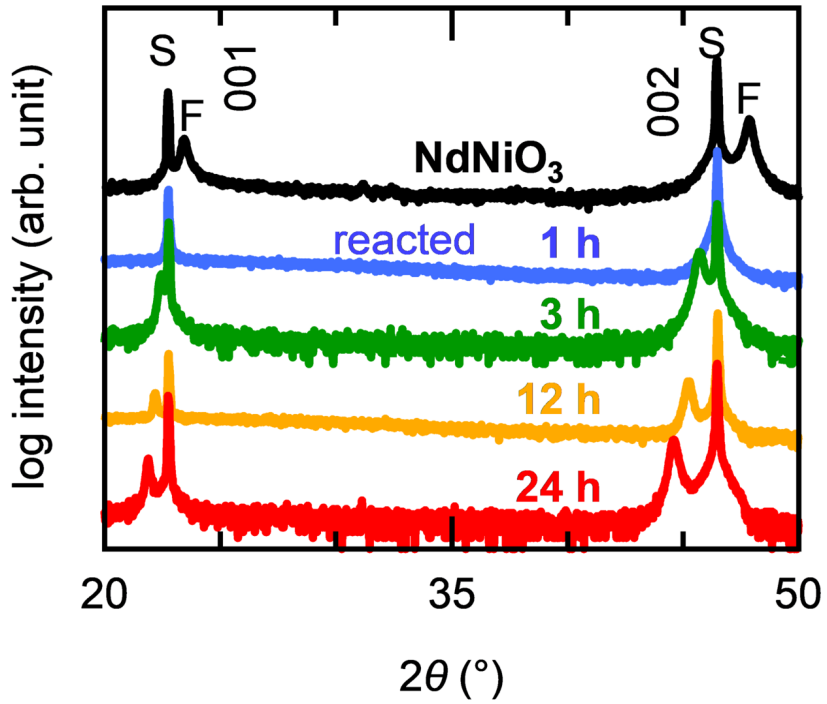

Figure 4-2. XRD 2θ–θ patterns of precursor $NdNiO_3$ and fluorinated films. S and F denote diffraction peaks related to $SrTiO_3$ substrate and film, respectively.

Figure 4-2 shows the out-of-plane 2θ–θ X-ray diffraction (XRD) pattern of a precursor $NdNiO_3$ film deposited on a $SrTiO_3$ (STO) (100) substrate as well as those of the thin films reacted with PVDF at 350 °C for 1, 3, 12, and 24 h. The XRD pattern of the precursor film (black line) shows the 002 diffraction peak of perovskite $NdNiO_3$ at $2\theta = 47.87°$. The out-of-plane lattice constant, c, was calculated to be 3.80 Å, which is in good agreement with previously reported values [95,96]. After the as-grown oxide films were treated with PVDF, the 002 diffraction peak steadily shifted to lower angles with an increase in the reaction time and was observed at 44.60° in the case of the film treated for 24 h, indicating that out-of-plane lattice expansion occurred after fluorination with PVDF.

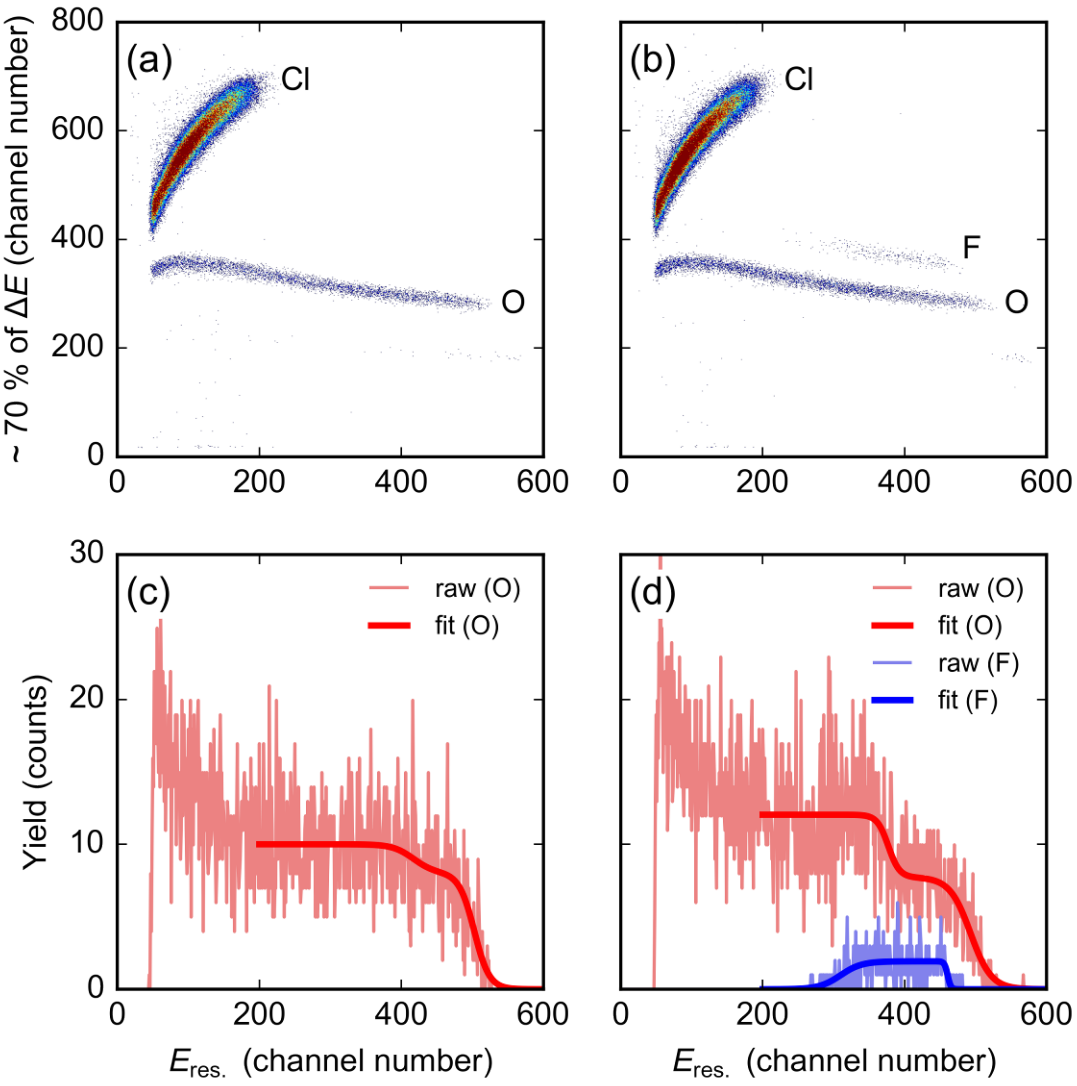

Figure 4-3. ΔE–$E_{res.}$ (residual energy) ERDA histograms of (a) $NdNiO_3/SrTiO_3$ and (b) $NdNiO_xF_y/SrTiO_3$ (12 h fluorination). (c) and (d) show spectra of O (F) recoils extracted from (a) and (b), respectively, along with the fitting results.

Next I investigated the amount of incorporated fluorine inside the reacted film. To determine the absolute chemical composition (x and y in $NdNiO_xF_y$), I performed the elastic-recoil detection analysis (ERDA) for the sample fluorinated for 12 h. Figure 4-3 shows ΔE–E histograms and extracted energy profile of oxygen and fluorine in the precursor and fluorinated samples. They are fitted with the following formula:

$$f_{\mathrm{O}}(E_{\mathrm{res}}) = \frac{C_1}{2}\left(\tanh\frac{E_{\mathrm{res}} - E_{\mathrm{interface}}}{w_{\mathrm{interface}}} - \tanh\frac{E_{\mathrm{res}} - E_{\mathrm{edge}}}{w_{\mathrm{edge}}}\right) + \frac{C_2}{2}\left(1 - \tanh\frac{E_{\mathrm{res}} - E_{\mathrm{interface}}}{w_{\mathrm{interface}}}\right),$$

$$f_{\mathrm{F}}(E_{\mathrm{res}}) = \frac{C_3}{2}\left(\tanh\frac{E_{\mathrm{res}} - E_{\mathrm{interface}}}{w_{\mathrm{interface}}} - \tanh\frac{E_{\mathrm{res}} - E_{\mathrm{edge}}}{w_{\mathrm{edge}}}\right).$$

Here, E_{res} is the independent variable, and E_{edge} and $E_{\mathrm{interface}}$ are the fitting parameters corresponding respectively to the channel numbers of the leading edge and interface. Further, w_{edge} and $w_{\mathrm{interface}}$ are the fitting parameters that signify the energy broadening at the leading edge and interface, respectively. Finally, C_1, C_2, and C_3 are the fitting parameters that represent the yields of O in the film, O in the substrate, and F in the film, respectively. Taking into account the stopping powers of the film and substrate materials for O and F and recoil cross sections and assuming the oxygen concentration in the as-grown oxide to be 3.0 ($NdNiO_3$), I derived the composition of the film after fluorination for 12 h to be $NdNiO_{2.1}F_{0.9}$. This indicates that the reaction between $NdNiO_3$ and PVDF causes the partial substitution of oxygen anions for fluoride anions; thus hereafter I assumed that the reaction yielded the oxyfluoride $NdNiO_{3-x}F_x$ for all the samples with different reaction time.

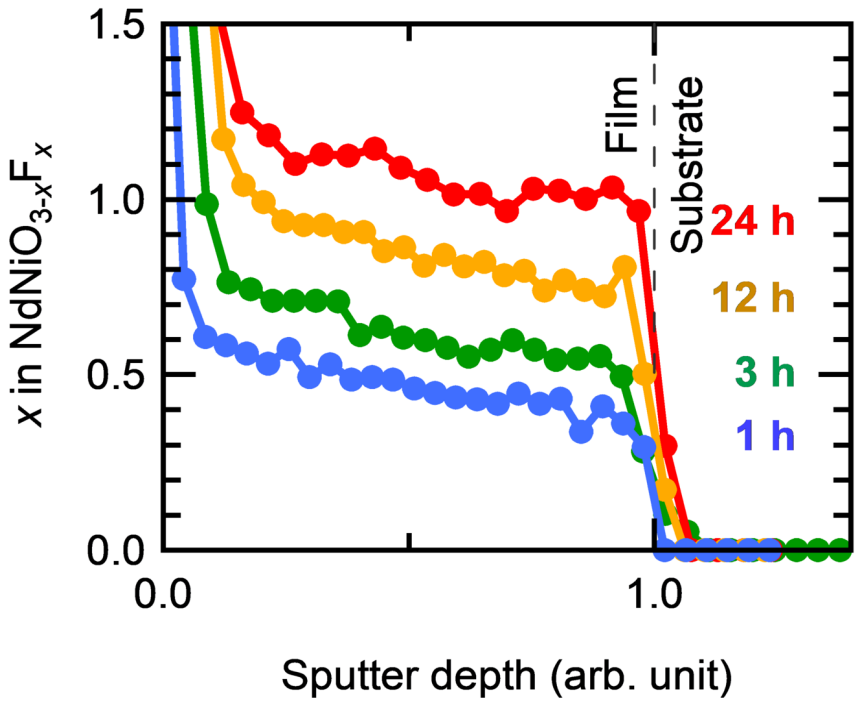

Figure 4-4. Depth-dependence of fluorine concentration as measured by XPS with Ar^+ sputtering. Film–substrate interface was determined as the location at which the intensities of the Nd, Ni, Sr, and Ti peak change abruptly.

The anion compositions of the films with different reaction time were compared by depth-resolved X-ray photoelectron spectroscopy (XPS) measurements, as shown in Figure 4-4. It was observed that, with an increase in the reaction time, fluorine atoms were gradually incorporated into the films, confirming that the films were successfully fluorinated and their fluorine content could be controlled by varying the reaction time. Obviously, the entire film, from the surface to the film/substrate interface, was fluorinated; although the topmost surface region had a higher fluorine concentration possibly due to small amounts of surface residues, the fluorine distribution inside the film was rather smooth. The change of the lattice constant as a function of the reaction time showed non-linear, sigmoid-like dependence (Figure 4-5a). The fluorine content inside the film was proportional to their lattice constant, obeying Vegard's law (Figure 4-5b).

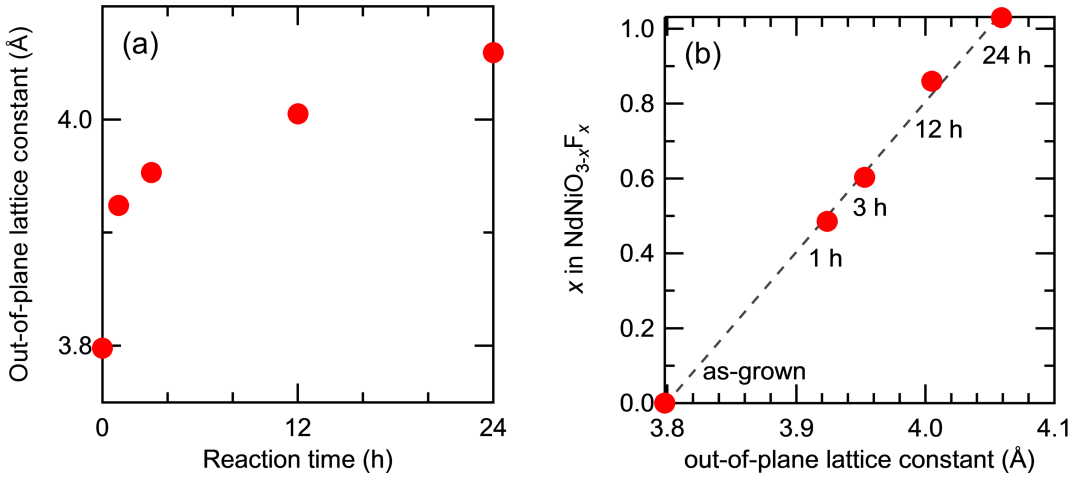

Figure 4-5. Relationships between (a) the out-of-plane lattice constants and the reaction time, and (b) fluorine content (x in $NdNiO_{3-x}F_{x}$) and the out-of-plane lattice constant. In the plot (b), the x values showed linear dependence on the lattice constants, obeying Vegard's law.

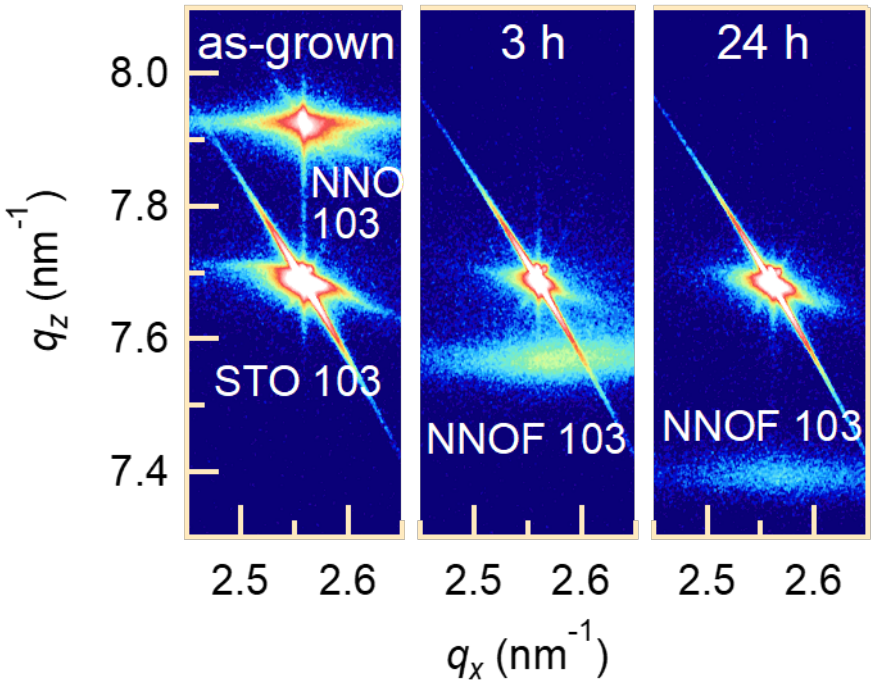

Figure 4-6. RSMs around the 103+ asymmetric diffraction for the as-grown film and those fluorinated for 3 and 24 h. NNO, STO, and NNOF represent $NdNiO_3$, $SrTiO_3$, and $NdNiO_{3-x}F_x$, respectively.

The reciprocal space maps (RSMs) around the 103+ asymmetric diffraction of the as-grown and fluorinated films were recorded (Figure 4-6). The q_x value (2.56 nm^{-1}) of the diffraction spot of the $NdNiO_3$ film was the same as that in the case of the substrate. That indicates that the film underwent epitaxial strain from the substrate, and the in-place lattice was at least partially locked to that of the substrate. While the out-of-plane coordinate, q_z, of the diffraction spot decreased after fluorination, the in-plane coordinate, q_x, showed almost no shifts, even though the peak itself became broader, which was indicative of a decrease in crystallinity. These observations suggest that the cube-on-cube epitaxial relationships between film and substrate lattice were unchanged during the low-temperature fluorination process.

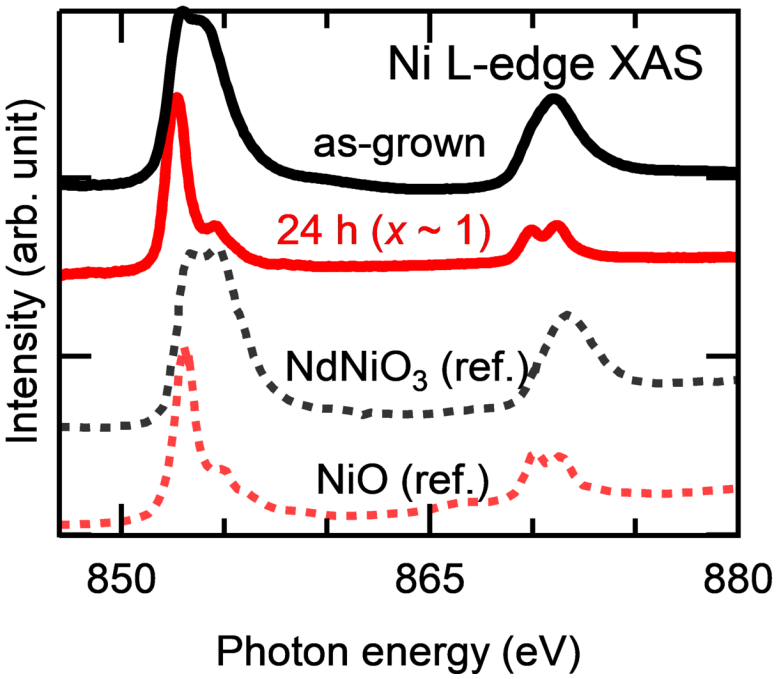

Figure 4-7. XAS spectra of as-grown and 24 h-fluorinated films. Dashed plots are taken from literature [97].

Although the ionic radius of F^- (133 pm) is smaller than that of O^{2-} (140 pm) [98], the lattice constants of the films increased after fluorination. This can be attributed to the

change in the chemical valence state of the nickel ions; the fluorine substitution process produces additional electrons, which reduce the nickel ions from Ni^{3+} to Ni^{2+}. These extra electrons enter the antibonding σ* (Ni 3d–O/F 2p) orbitals, increasing the length of the bonds between the nickel atoms and the anions. To confirm the valence associated with fluorination, I performed Ni L-edge XAS measurements, as shown in Figure 4-7. It is known [97] that the Ni 2p XAS spectrum of Ni^{3+} is very different from that of Ni^{2+}. Figure 4-7 also shows the XAS spectra from previous studies as references. Obviously, the spectrum of the as-grown film resembles that of $NdNi^{3+}O_3$. On the other hand, the spectrum changes to that corresponding to Ni^{2+} after fluorination, supporting the above-mentioned claim that the nickel ions undergo reduction and that their valence state changes from +3 to +2 upon fluorine substitution.

Next, I discuss the electrical and optical properties of the $NdNiO_{3-x}F_x$ thin films. After fluorination for 3 h, the film sheet resistance increased dramatically, from 3×10^2 Ω/sq. to ~ 1×10^9 Ω/sq. The latter value was comparable to the resistance of the insulating STO substrates, which made it difficult to investigate the intrinsic electrical transport properties of the $NdNiO_{3-x}F_x$ thin films. A similarly large change in resistivity, of more than six orders of magnitude, was also observed during the annealing of $NdNiO_3$ in an ultra-high vacuum [93]. Figure 4-8 shows the optical absorption coefficients, α, of the $NdNiO_{3-x}F_x$ films as functions of the incident photon energy. For energies lower than 3.0 eV, α decreased monotonically with an increase in the reaction time, suggesting that the carrier density was reduced significantly by fluorine substitution. The linear onset of the $(\alpha h\nu)^n$–$(h\nu)$ plot (Tauc plot), where $n = 2$ (direct transition), was extrapolated as per a previous study [93]; this yielded optical bandgap values of 0.84, 0.95, and 2.1 eV (with 0.2–0.3 eV uncertainty as to which part of the slope should be seen as “a linear onset”) for the 3-, 12-, and 24-h fluorinated samples, respectively. These results imply that the fluorination of $NdNiO_3$ opens a finite bandgap of more than 1 eV, a conclusion that is

consistent with the abrupt increase observed in the resistivity.

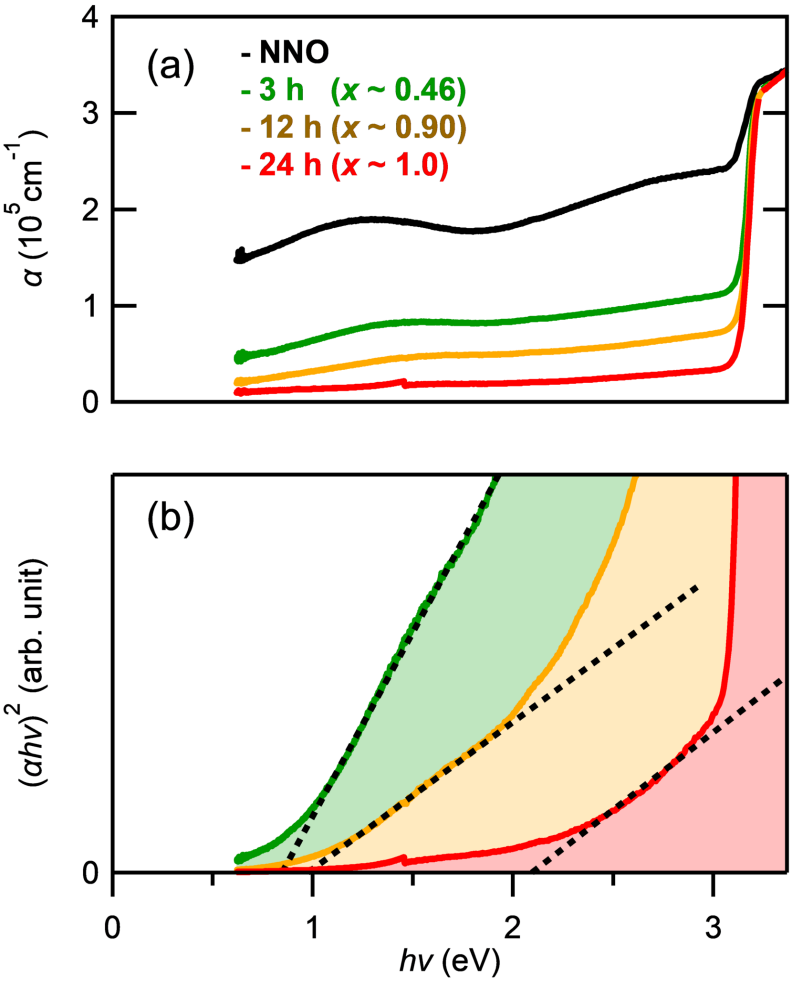

Figure 4-8. (a) Optical absorption coefficients, α, of $NdNiO_3$ and $NdNiO_{3-x}F_x$ thin films prepared using different reaction time. (b) Tauc ($(\alpha hv)^2$ versus hv) plots of insulating films assuming a direct transition. Strong absorption at energies greater than 3 eV is owing to the STO substrate (bandgap: 3.2 eV).

The extremely high increases in the resistance resulting from the fluorination process as well as large bandgap opening of 2.1 eV suggest that the process induces drastic changes in the electronic states of the thin films. Thus, in order to investigate the electronic states, I performed bulk-sensitive HAXPES. The Nd 3d core-level spectra are shown in Figure 4-9. In the 3d spectra of the rare earth elements, different satellite peaks

(marked by triangles) can be observed; these are attributable to the interactions between the generated core holes and the valence electrons [99]. In the case of the $NdNiO_3$ film, a satellite peak is observed at a binding energy (E_b) smaller than that corresponding to the main peak. This peak is called a "shake-down," or "well-screened" satellite peak and is characteristic of metallic compounds. After the fluorination of the films, this shake-down peak disappears and a new spectral weight emerges at a larger E_b. The latter, which is called a "shake-up" satellite peak, is characteristic of insulating compounds and appears when the valence electrons are transferred to the 4f levels inside the gap, thus corroborating the claim that $NdNiO_3$ undergoes the MIT driven by fluorine substitution. Note that the Nd 3d5/2 main peak was observed around 983 eV for all the samples, indicating that the Nd ions remained trivalent throughout the fluorination process.

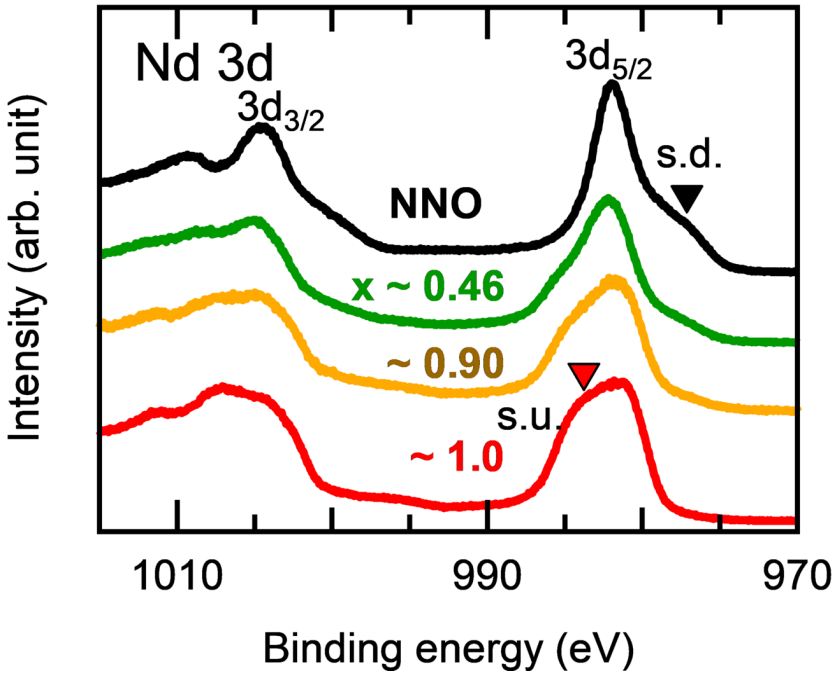

Figure 4-9. Nd 3d HAXPES spectra of $NdNiO_3$ and $NdNiO_{3-x}F_x$ films measured at 300 K. Annotations "s.d." and "s.u." stand for "shake-down" and "shake-up" satellite, respectively

The Ni 2p core-level photoelectron spectra are shown in Figure 4-10. Each spectrum is characterized by $2p_{3/2}$–$2p_{1/2}$ spin-orbit separation and satellite peaks. The E_b value of the Ni 2p peaks is influenced by both the chemical valence of Ni and the counter anions (O^{2-} versus F^-). That is to say, the reduction of Ni^{3+} to Ni^{2+} in the oxides lowers the E_b value [100–103], while the isovalent substitution of NiO for NiF_2 increases the E_b value [103]. As can be seen in Figure 4-10, the spectral weight shifts to a higher E_b after reductive fluorine substitution, indicating that the effect of the counter anions and not the change in the chemical valence is the dominating factor in the case of $NdNiO_{3-x}F_x$.

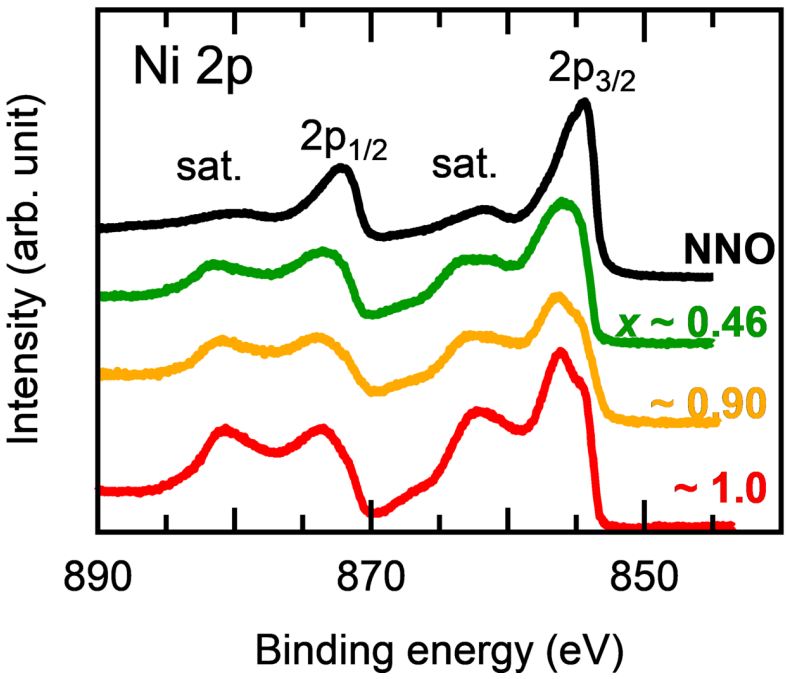

Figure 4-10. Ni 2p HAXPES spectra of $NdNiO_3$ and $NdNiO_{3-x}F_x$ films measured at 300 K. "sat." indicates satellite peaks.

Figure 4-11 shows the valence-band HAXPES spectra of the $NdNiO_3$ and $NdNiO_{3-x}F_x$ films. In the spectrum of the precursor $NdNiO_3$ film (black curve), the features located at lower binding energies (features a and b) can primarily be attributed to the contribution of the Ni 3d orbital, while those at larger binding energies (features c

and d) are mainly owing to the O 2p orbital [104]. A finite density of states is observed at E_F; this is consistent with the experimentally observed metallic conduction at room temperature. Further, after fluorination, features (a) and (b) disappeared, and the density of states at E_F reduced to zero with a bandgap opening, suggesting that the perovskite nickel oxyfluorides are electrically insulating. This change indicates that the insulating characteristics of the $NdNiO_{3-x}F_x$ thin films are induced by a Mott-type gap opening and not by rigid-band shifting. In addition, a new spectral structure (e) emerges at an E_b value higher than those of the O 2p-nature states. Considering that the electronegativity of fluorine is higher than that of oxygen, I believe that this feature originates from the F 2p-derived states. Indeed, its relative intensity increased with the fluorine content, while the oxygen-related peaks were suppressed, confirming the substitution of fluorine for oxygen.

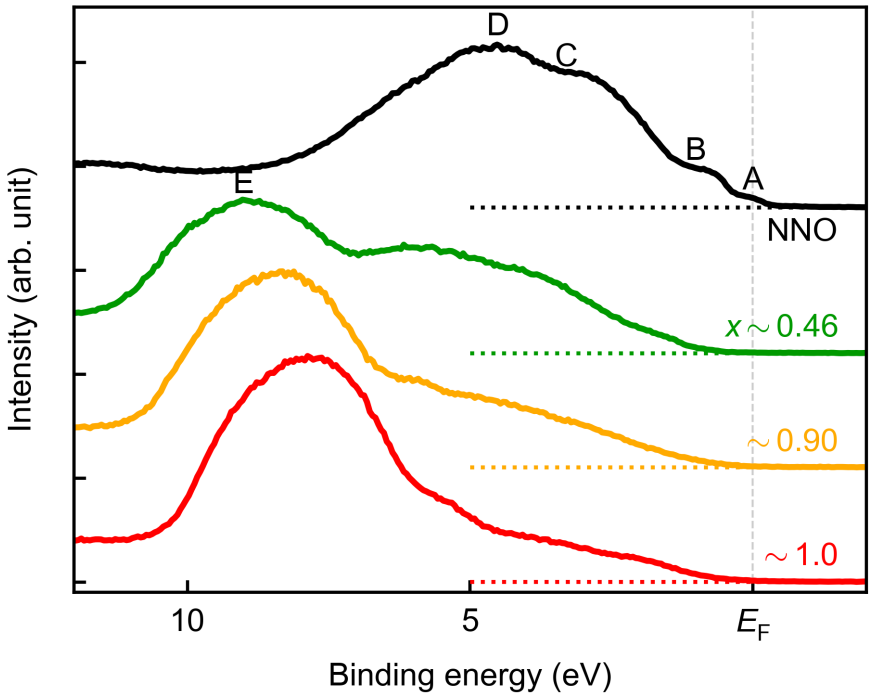

Figure 4-11. Valence band HAXPES spectra of $NdNiO_3$ and $NdNiO_{3-x}F_x$ thin films measured at 300 K.

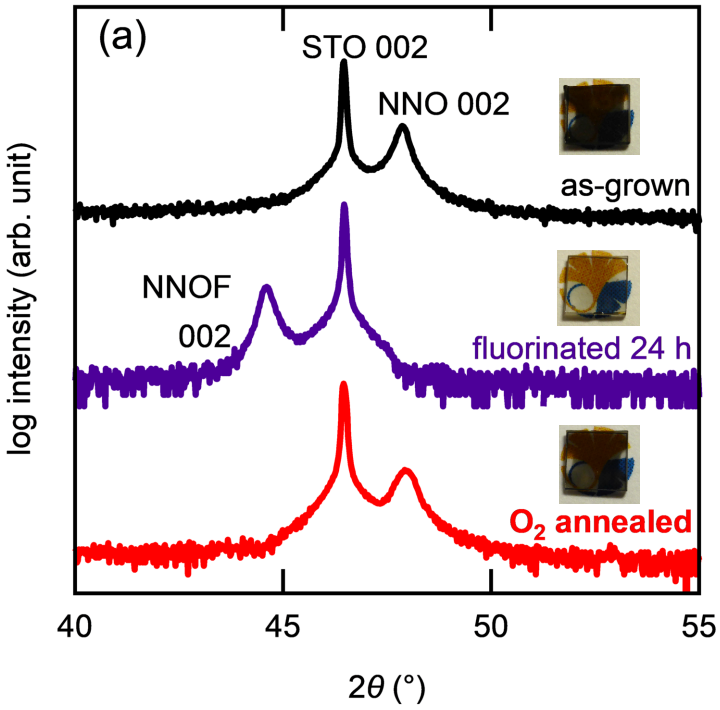

Figure 4-12. XRD 2θ–θ patterns of as-grown, 24-h fluorinated, and oxygen-annealed (450 °C for 5 h) films.

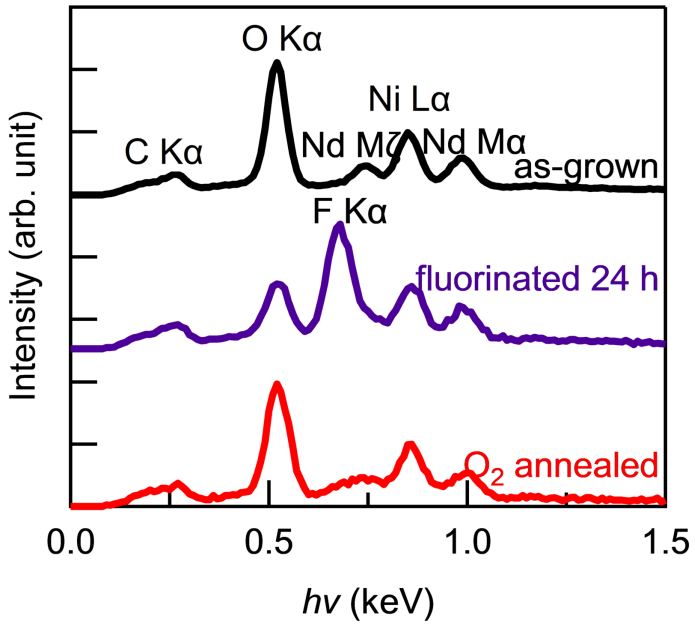

Figure 4-13. SEM-EDS spectra of as-grown, fluorinated for 24 h, and oxygen-annealed films. Annealing was performed at 450 °C for 5 h. Electron accelerating voltage was set at 2.5 keV for these measurements.

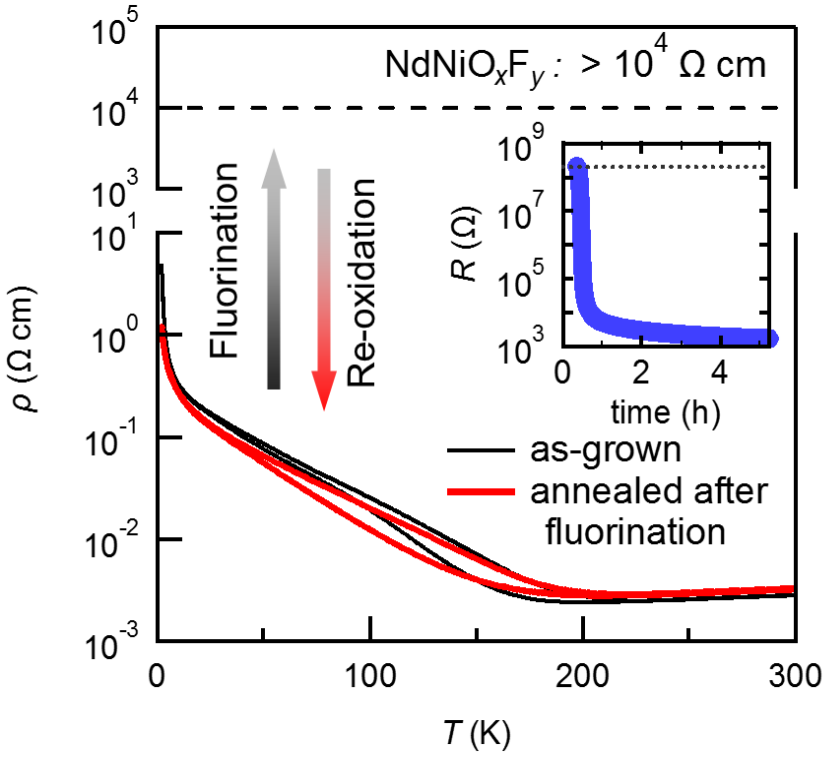

Figure 4-14. Electrical resistivity versus temperature plots of as-grown film and oxygen-annealed film after fluorination. Inset shows electrical resistance measured in situ during oxygen annealing process.

Finally, I discuss the reversibility of the fluorination process. Figure 4-12 shows the 2θ–θ patterns of the as-grown $NdNiO_3$ film, the 24-h fluorinated $NdNiO_{3-x}F_x$ film, and an $NdNiO_{3-x}F_x$ film annealed in oxygen at 10^5 Pa for 5 h at 450 °C. Notably, the lattice constant of the annealed film reverted to that of the as-grown $NdNiO_3$ film, suggesting that fluoride ions were released during the annealing of the film in oxygen while the cation framework was maintained. In fact, a negligible amount of fluorine was observed within this film by energy dispersive X-ray spectroscopic (EDS) analysis (Figure 4-13). The reversible nature of the phase transformation seems surprising because possibly stronger Ni–F bonds are replaced by Ni–O bonds during oxygen annealing. I speculate that the change in the chemical oxidation state of nickel ions plays an important role in the formation of Ni-F or Ni-O bonds. During the reductive fluorination, electrons are added

to the Ni^{3+} ions, promoting the Ni–O bond breaking and the formation of Ni–F bonds. On the other hand, during the oxygen annealing, loss of electrons from the Ni^{2+} ions breaks the Ni–F bonds. In situ monitoring of the film resistance during the oxygen annealing process (see inset in Figure 4-14) revealed an exponential decrease in the film resistivity down to a value comparable to that of the as-grown film. Figure 4-14 plots the resistivity versus temperature curves for the as-grown and oxygen-annealed films. Both curves indicate that the MIT occurs at ~200 K and the curves overlap very well. Note that the resistivity of the fluorinated film was higher than 10^4 Ω cm (~ 1.0 GΩ /sq.). As shown in the inset of Figure 4-12, the black color of the $NdNiO_3$ film faded and the film became transparent after fluorination for 24 h. However, the film became black again after the oxygen-annealing process. These observations confirm that topotactic reversible fluorination is an effective method for modulating electrical conduction in metal-oxide thin films and thus can be used for synthesizing films suitable for resistance-switching applications.

4.4 Conclusions

I investigated the effects of fluorine doping of $NdNiO_3$ thin films using PVDF. After reacting with PVDF, $NdNiO_3$ epitaxial thin films grown on $SrTiO_3$ substrates transformed into films of $NdNiO_{3-x}F_x$, where the fluorine content, x, could be controlled by varying the reaction time. The fluorination of the films resulted in a significant increase in the electrical resistance of more than six orders of magnitude. Furthermore, XAS and HAXPES measurements suggested that a Mott-type gap opening is the cause of the extremely high resistance increase associated with the fluorination process. I also found that the resistance of the fluorinated thin films returned to the original value when the films were annealed in an oxygen atmosphere. The reversible resistance modulation of $NdNiO_3$ may lead to device applications, e.g., in thermal or atmospheric sensors. Since it

can be performed without expensive setups like ultra-high vacuum or microfabrication, the reversible fluorination/oxidation of transition-metal oxides would pave the way for the discovery of new physical properties in various transition metal oxides.

Chapter 5. Fluorination of lanthanum cuprates $LaCuO_x$: observation of metallic conduction

本章については、5年以内に雑誌等で刊行予定のため、非公開。

Chapter 6. General conclusions

In this thesis, I studied modification of structures and properties of transition-metal oxide thin films by soft chemical processes. Using topotactic hydrogen and fluorine incorporation, I achieved following things.

In Chapter 3, I reported soft chemical reactions between $NdNiO_3$ thin films and CaH_2.In spite of previous researches based on bulk powder samples, H^- was incorporated to the crystal, and defect-fluorite structured $NdNiO_xH_y$ (x, $y \approx 2.3$, 0.7) films were obtained. A large amount of incorporated hydrogen suggested potential application for hydrogen storage. I also found that the structural features of the films, or more concretely, the crystal orientations, strongly depended on the reaction temperature. After low-temperature reaction at 240 °C, the oxyhydride grew in [001]-orientation with interfacial layer of infinite-layer oxide $NdNiO_2$. On the other hand, higher-temperature reaction at 400 °C resulted in [110]-orientation, though it seemed more poorly lattice-matched to the substrate than [001]-orientation. This kind of crystal growth against epitaxially stable configuration may indicate importance of kinetic factors like ionic diffusion, during topotactic reactions.

In Chapter 4, I investigated a different kind of topotactic reactions, i.e. fluorination, on the same precursor material, $NdNiO_3$. Here, the reaction products with polyvinylidene fluoride were perovskite oxyfluoride $NdNiO_{3-x}F_x$, where a part of oxygen in the precursor material is substituted by fluorine atoms. In this reaction, the amount of incorporated fluorine was systematically controlled by changing reaction time. I also investigated electronic properties of the obtained films and found that the oxyfluoride samples were highly insulating with band gap of 1–2 eV, possibly because of the strong Coulomb repulsion between electrons incorporated as a result of fluorine substitution. Another important finding is that the fluorinated films could be reverted to $NdNiO_3$ by heating

under oxygen atmosphere. This allows reversible switching between low-resistance state ($NdNiO_3$) and high-resistance state ($NdNiO_{3-x}F_x$). This behavior may lead to development of new switching devices based on topotactic incorporation of fluorine. Also, fluorination of transition-metal oxides would pave the way for discovering new physical properties in various transition-metal oxides as it does not require expensive setups like ultra-high vacuum or microfabrication.

In Chapter 5, I focused on different starting material $LaCuO_x$ and aimed to obtain novel oxyfluoride that allows metallic conduction. In the first part of the chapter, I investigated thin-film growth of $LaCuO_x$ itself. It showed complex domain patterns composed of narrow wall-like nanostructures, which was controllable by changing lattice symmetry of the substrate. Because of the stripe-like domains, the films on $NdGaO_3$ (110) showed anisotropic conduction along and across the domains. For fluorination, I found that CuF_2 was an effective fluorine source and synthesized oxyfluoride $LaCuO_xF_y$ with (averaged) composition of (x, $y \approx 2.0$, 0.94). Although the chemical composition inside the film was not homogeneous, the fluorinated sample showed metallic conduction, which was quite rare as perovskite-structured oxyfluorides.

In conclusion, I applied soft chemical processes on transition-metal oxide epitaxial thin films, $NdNiO_3$ and $LaCuO_x$. As discussed above, the structures and properties of the transition-metal oxides can greatly be altered by hydrogen and fluorine doping via these processes. The findings in this study demonstrate that the soft chemical processes for thin films are effective for discovering novel materials and exploring their physical properties.

Bibliography

[1] M. Imada, A. Fujimori, and Y. Tokura, Rev. Mod. Phys. **70**, 1039 (1998).

[2] M. P. M. Dean, G. Dellea, R. S. Springell, F. Yakhou-Harris, K. Kummer, N. B. Brookes, X. Liu, Y.-J. Sun, J. Strle, T. Schmitt, L. Braicovich, G. Ghiringhelli, I. Božović, and J. P. Hill, Nat. Mater. **12**, 1019 (2013).

[3] A. Urushibara, Y. Moritomo, T. Arima, A. Asamitsu, G. Kido, and Y. Tokura, Phys. Rev. B **51**, 14103 (1995).

[4] K. G. S. Ranmohotti, E. Josepha, J. Choi, J. Zhang, and J. B. Wiley, Adv. Mater. **23**, 442 (2011).

[5] K. Toda, M. Takahashi, T. Teranishi, Z. Ye, M. Sato, and Y. Hinatsu, J. Mater. Chem. **9**, 799 (1999).

[6] M. A. Hayward, M. A. Green, M. J. Rosseinsky, and J. Sloan, J. Am. Chem. Soc. **121**, 8843 (1999).

[7] J. Choi, X. Zhang, and J. B. Wiley, Inorg. Chem. **48**, 4811 (2009).

[8] K. Mizushima, P. C. Jones, P. J. Wiseman, and J. B. Goodenough, Mater. Res. Bull. **15**, 783 (1980).

[9] C. Jin-Ho, K. Dong-Kuk, P. Nam-Gyu, K. Dong-Hoon, H. Seong-Ju, and H. Sung-Ho, Phys. C Supercond. **235**–**240**, 1023 (1994).

[10] Z. S. Gönen, D. Paluchowski, P. Zavalij, B. W. Eichhorn, and J. Gopalakrishnan, Inorg. Chem. **45**, 8736 (2006).

[11] K. Momma and F. Izumi, J. Appl. Crystallogr. **44**, 1272 (2011).

[12] J. Jorgensen, B. Dabrowski, S. Pei, D. Hinks, L. Soderholm, B. Morosin, J. Schirber, E. Venturini, and D. Ginley, Phys. Rev. B **38**, 11337 (1988).

[13] F. Girgsdies and R. Schöllhorn, Solid State Commun. **91**, 111 (1994).

[14] J. Jorgensen, B. Dabrowski, S. Pei, D. Richards, and D. Hinks, Phys. Rev. B **40**,

2187 (1989).

[15] B. Chevalier, A. Tressaud, B. Lepine, K. Amine, J. M. Dance, L. Lozano, E. Hickey, and J. Etourneau, Phys. C Supercond. **167**, 97 (1990).

[16] R. Li and C. Greaves, Phys. Rev. B **62**, 3811 (2000).

[17] L. D. Aikens, L. J. Gillie, R. K. Li, and C. Greaves, J. Mater. Chem. **12**, 264 (2002).

[18] M. Al-Mamouri, P. P. Edwards, C. Greaves, and M. Slaski, Nature **369**, 382 (1994).

[19] J. Briático, B. Alascio, R. Allub, A. Butera, A. Caneiro, M. Causa, and M. Tovar, Phys. Rev. B **53**, 14020 (1996).

[20] G. Zampieri, F. Prado, A. Caneiro, J. Briático, M. Causa, M. Tovar, B. Alascio, M. Abbate, and E. Morikawa, Phys. Rev. B **58**, 3755 (1998).

[21] B. Raveau, C. Michel, M. Hervieu, and A. Maignan, J. Mater. Chem. **5**, 803 (1995).

[22] M. J. Martínez-Lope, M. . Casais, and J. A. Alonso, J. Alloys Compd. **275**–**277**, 109 (1998).

[23] T. Moriga, O. Usaka, I. Nakabayashi, Y. Hirashima, T. Kohno, S. Kikkawa, and F. Kanamaru, Solid State Ionics **74**, 211 (1994).

[24] M. Crespin, P. Levitz, and L. Gatineau, J. Chem. Soc. Faraday Trans. 2 **79**, 1181 (1983).

[25] M. A. Hayward, Chem. Mater. **17**, 670 (2005).

[26] J. J. Adkin and M. A. Hayward, Inorg. Chem. **47**, 10959 (2008).

[27] Y. Tsujimoto, C. Tassel, N. Hayashi, T. Watanabe, H. Kageyama, K. Yoshimura, M. Takano, M. Ceretti, C. Ritter, and W. Paulus, Nature **450**, 1062 (2007).

[28] Y. Kobayashi, Z. Li, K. Hirai, C. Tassel, F. Loyer, N. Ichikawa, N. Abe, T.

Yamamoto, Y. Shimakawa, K. Yoshimura, M. Takano, O. J. Hernandez, and H. Kageyama, J. Solid State Chem. **207**, 190 (2013).

[29] M. A. Hayward, E. J. Cussen, J. B. Claridge, M. Bieringer, M. J. Rosseinsky, C. J. Kiely, S. J. Blundell, I. M. Marshall, and F. L. Pratt, Science (80-.). **295**, 1882 (2002).

[30] F. W. Poulsen, Solid State Ionics **145**, 387 (2001).

[31] R. M. Helps, N. H. Rees, and M. A. Hayward, Inorg. Chem. **49**, 11062 (2010).

[32] T. Sakaguchi, Y. Kobayashi, T. Yajima, M. Ohkura, C. Tassel, F. Takeiri, S. Mitsuoka, H. Ohkubo, T. Yamamoto, J. E. Kim, N. Tsuji, A. Fujihara, Y. Matsushita, J. Hester, M. Avdeev, K. Ohoyama, and H. Kageyama, Inorg. Chem. **51**, 11371 (2012).

[33] Y. Kobayashi, O. J. Hernandez, T. Sakaguchi, T. Yajima, T. Roisnel, Y. Tsujimoto, M. Morita, Y. Noda, Y. Mogami, A. Kitada, M. Ohkura, S. Hosokawa, Z. Li, K. Hayashi, Y. Kusano, J. E. Kim, N. Tsuji, A. Fujiwara, Y. Matsushita, K. Yoshimura, K. Takegoshi, M. Inoue, M. Takano, and H. Kageyama, Nat. Mater. **11**, 1 (2012).

[34] T. Yamamoto, R. Yoshii, G. Bouilly, Y. Kobayashi, K. Fujita, Y. Kususe, Y. Matsushita, K. Tanaka, and H. Kageyama, Inorg. Chem. **54**, 1501 (2015).

[35] F. Denis Romero, A. Leach, J. S. Möller, F. Foronda, S. J. Blundell, and M. A. Hayward, Angew. Chem. Int. Ed. Engl. **53**, 7556 (2014).

[36] T. Katayama, A. Chikamatsu, H. Kamisaka, Y. Yokoyama, Y. Hirata, H. Wadati, T. Fukumura, and T. Hasegawa, AIP Adv. **5**, 107147 (2015).

[37] J. Bang, S. Matsuishi, H. Hiraka, F. Fujisaki, T. Otomo, S. Maki, J. I. Yamaura, R. Kumai, Y. Murakami, and H. Hosono, J. Am. Chem. Soc. **136**, 7221 (2014).

[38] C. A. Bridges, G. R. Darling, M. A. Hayward, and M. J. Rosseinsky, J. Am. Chem. Soc. **127**, 5996 (2005).

[39] H. Takahashi, K. Igawa, K. Arii, Y. Kamihara, M. Hirano, and H. Hosono, Nature **453**, 376 (2008).

[40] Y. Tsujimoto, K. Yamaura, and T. Uchikoshi, Inorg. Chem. **52**, 10211 (2013).

[41] Y. Kobayashi, M. Tian, M. Eguchi, and T. E. Mallouk, J. Am. Chem. Soc. **131**, 9849 (2009).

[42] M. G. Francesconi, P. R. Slater, J. P. Hodges, C. Greaves, P. P. Edwards, M. Al-Mamouri, and M. Slaski, J. Solid State Chem. **135**, 17 (1998).

[43] M. H. Delville, D. Barbut, A. Wattiaux, J. Bassat, M. Ménétrier, C. Labrugère, J. C. Grenier, and J. Etourneau, Inorg. Chem. **48**, 7962 (2009).

[44] O. Clemens, C. Rongeat, M. A. Reddy, A. Giehr, M. Fichtner, and H. Hahn, Dalton Trans. **43**, 15771 (2014).

[45] P. R. Slater, J. Fluor. Chem. **117**, 43 (2002).

[46] T. Katayama, A. Chikamatsu, Y. Hirose, T. Fukumura, and T. Hasegawa, J. Sol-Gel Sci. Technol. (2014).

[47] M. Kawai, S. Inoue, M. Mizumaki, N. Kawamura, N. Ichikawa, and Y. Shimakawa, Appl. Phys. Lett. **94**, 82102 (2009).

[48] D. Kaneko, K. Yamagishi, A. Tsukada, T. Manabe, and M. Naito, Phys. C Supercond. **469**, 936 (2009).

[49] T. Katayama, A. Chikamatsu, Y. Hirose, R. Takagi, H. Kamisaka, T. Fukumura, and T. Hasegawa, J. Mater. Chem. C **2**, 5350 (2014).

[50] F. J. Berry, R. Heap, Ö. Helgason, E. A. Moore, S. Shim, P. R. Slater, and M. F. Thomas, J. Phys. Condens. Matter **20**, 215207 (2008).

[51] G. Bouilly, T. Yajima, T. Terashima, Y. Kususe, K. Fujita, C. Tassel, T. Yamamoto, K. Tanaka, Y. Kobayashi, and H. Kageyama, CrystEngComm **16**, 9669 (2014).

[52] R. Eason, editor , *Pulsed Laser Deposition of Thin Films* (John Wiley & Sons,

Inc., Hoboken, NJ, USA, 2006).

[53] K. M. Satyalakshmi, R. M. Mallya, K. V. Ramanathan, X. D. Wu, B. Brainard, D. C. Gautier, N. Y. Vasanthacharya, and M. S. Hegde, Appl. Phys. Lett. **62**, 1233 (1993).

[54] M. M. Hirschler, Eur. Polym. J. **18**, 463 (1982).

[55] A. J. Pidduck, J. Anal. Appl. Pyrolysis **7**, 215 (1985).

[56] B. B. He, U. Preckwinkel, and K. L. Smith, Adv. X-Ray Anal. **43**, 273 (2000).

[57] N. D. Browning, I. Arslan, P. Moeck, and T. Topuria, Phys. Status Solidi **227**, 229 (2001).

[58] F. Reinert and S. Hüfner, New J. Phys. **7**, 97 (2005).

[59] M. P. Seah and W. A. Dench, Surf. Interface Anal. **1**, 2 (1979).

[60] I. Harayama, K. Nagashima, Y. Hirose, H. Matsuzaki, and D. Sekiba, Nucl. Instruments Methods Phys. Res. B **384**, 61 (2016).

[61] T. Yamamoto and H. Kageyama, Chem. Lett. 946 (2013).

[62] M. A. Hayward, in *Compr. Inorg. Chem. II*, edited by J. Reedijk and K. Poeppelmeier (Elsevier, 2013), pp. 417–453.

[63] M. A. Hayward and M. J. Rosseinsky, Solid State Sci. **5**, 839 (2003).

[64] V. V Poltavets, K. A. Lokshin, S. Dikmen, M. Croft, T. Egami, and M. Greenblatt, J. Am. Chem. Soc. **128**, 9050 (2006).

[65] F. D. Romero, S. J. Burr, J. E. McGrady, D. Gianolio, G. Cibin, and M. A. Hayward, J. Am. Chem. Soc. **135**, 1838 (2013).

[66] M. A. Hayward and M. J. Rosseinsky, Chem. Mater. **12**, 2182 (2000).

[67] S. Inoue, M. Kawai, Y. Shimakawa, M. Mizumaki, N. Kawamura, T. Watanabe, Y. Tsujimoto, H. Kageyama, and K. Yoshimura, Appl. Phys. Lett. **92**, 161911 (2008).

[68] T. Matsuyama, A. Chikamatsu, Y. Hirose, T. Fukumura, and T. Hasegawa,

Appl. Phys. Express **4**, 13001 (2011).

[69] T. Yajima, A. Kitada, Y. Kobayashi, T. Sakaguchi, G. Bouilly, S. Kasahara, T. Terashima, M. Takano, and H. Kageyama, J. Am. Chem. Soc. **134**, 8782 (2012).

[70] T. Katayama, A. Chikamatsu, Y. Hirose, H. Kumigashira, T. Fukumura, and T. Hasegawa, J. Phys. D. Appl. Phys. **47**, 135304 (2014).

[71] M. Medarde, C. Dallera, M. Grioni, B. Delley, F. Vernay, J. Mesot, M. Sikora, J. A. Alonso, and M. J. Martínez-Lope, Phys. Rev. B **80**, 245105 (2009).

[72] P.-H. Xiang, N. Zhong, C.-G. Duan, X. D. Tang, Z. G. Hu, P. X. Yang, Z. Q. Zhu, and J. H. Chu, J. Appl. Phys. **114**, 243713 (2013).

[73] M. Stewart, J. Liu, M. Kareev, J. Chakhalian, and D. Basov, Phys. Rev. Lett. **107**, 176401 (2011).

[74] Y. Krockenberger, K. Sakuma, and H. Yamamoto, Appl. Phys. Express **5**, 43101 (2012).

[75] M. Widerøe, H. Fjellvåg, T. Norby, F. Willy Poulsen, and R. Willestofte Berg, J. Solid State Chem. **184**, 1890 (2011).

[76] M. Kawai, K. Matsumoto, N. Ichikawa, M. Mizumaki, O. Sakata, N. Kawamura, S. Kimura, and Y. Shimakawa, Cryst. Growth Des. **10**, 2044 (2010).

[77] S. Inoue, M. Kawai, N. Ichikawa, H. Kageyama, W. Paulus, and Y. Shimakawa, Nat. Chem. **2**, 213 (2010).

[78] D. N. Basov, R. D. Averitt, D. van der Marel, M. Dressel, and K. Haule, Rev. Mod. Phys. **83**, 471 (2011).

[79] J. Wang, J. B. Neaton, H. Zheng, V. Nagarajan, S. B. Ogale, B. Liu, D. Viehland, V. Vaithyanathan, D. G. Schlom, U. V Waghmare, N. A. Spaldin, K. M. Rabe, M. Wuttig, and R. Ramesh, Science **299**, 1719 (2003).

[80] Y. Tokura, Y. Taguchi, Y. Okada, Y. Fujishima, T. Arima, K. Kumagai, and Y. Iye, Phys. Rev. Lett. **70**, 2126 (1993).

[81] J. G. Bednorz and K. A. Müller, Zeitschrift Für Phys. B Condens. Matter **64**, 189 (1986).

[82] M. L. Medarde, J. Phys. Condens. Matter **9**, 1679 (1997).

[83] G. Catalan, Phase Transitions **81**, 729 (2008).

[84] J. A. Alonso, M. J. Martínez-Lope, M. T. Casais, M. A. G. Aranda, and M. T. Fernández-Díaz, J. Am. Chem. Soc. **121**, 4754 (1999).

[85] J. A. Alonso and J. L. García-Muñoz, Phys. Rev. Lett. **82**, 3871 (1999).

[86] J. A. Alonso, M. J. Martínez-Lope, M. T. Casais, and M. T. Fernández-Díaz, Phys. Rev. B **61**, 1756 (2000).

[87] U. Staub, G. I. Meijer, F. Fauth, R. Allenspach, J. G. Bednorz, J. Karpinski, S. M. Kazakov, L. Paolasini, and F. D'Acapito, Phys. Rev. Lett. **88**, 126402 (2002).

[88] S. Asanuma, P.-H. Xiang, H. Yamada, H. Sato, I. H. Inoue, H. Akoh, A. Sawa, K. Ueno, H. Shimotani, H. Yuan, M. Kawasaki, and Y. Iwasa, Appl. Phys. Lett. **97**, 142110 (2010).

[89] R. Scherwitzl, P. Zubko, I. G. Lezama, S. Ono, A. F. Morpurgo, G. Catalan, and J.-M. Triscone, Adv. Mater. **22**, 5517 (2010).

[90] J. García-Muñoz, M. Suaaidi, M. Martínez-Lope, and J. A. Alonso, Phys. Rev. B **52**, 13563 (1995).

[91] J. Shi, Y. Zhou, and S. Ramanathan, Nat. Commun. **5**, 4860 (2014).

[92] J. Chen, Y. Zhou, S. Middey, J. Jiang, N. Chen, L. Chen, X. Shi, M. Döbeli, J. Shi, J. Chakhalian, and S. Ramanathan, Appl. Phys. Lett. **107**, 31905 (2015).

[93] L. Wang, S. Dash, L. Chang, L. You, Y. Feng, X. He, K. Jin, Y. Zhou, H. G. Ong, P. Ren, S. Wang, L. Chen, and J. Wang, ACS Appl. Mater. Interfaces **8**, 9769 (2016).

[94] E. J. Moon, Y. Xie, E. D. Laird, D. J. Keavney, C. Y. Li, and S. J. May, J. Am. Chem. Soc. **136**, 2224 (2014).

[95] Y. Wang, F.-T. Huang, X. Luo, B. Gao, and S.-W. Cheong, Adv. Mater. (2016).

[96] F. Capon, D. Horwat, J. F. Pierson, M. Zaghrioui, and P. Laffez, J. Phys. D. Appl. Phys. **42**, 182006 (2009).

[97] M. Medarde, A. Fontaine, J. L. García-Muñoz, J. Rodríguez-Carvajal, M. de Santis, M. Sacchi, G. Rossi, and P. Lacorre, Phys. Rev. B **46**, 14975 (1992).

[98] R. D. Shannon, Acta Crystallogr. Sect. A **32**, 751 (1976).

[99] C. Bonnelle and Nissan Spector, *Rare-Earths and Actinides in High Energy Spectroscopy*, 1st ed. (Springer, 2015).

[100] A. P. Grosvenor, M. C. Biesinger, R. S. C. Smart, and N. S. McIntyre, Surf. Sci. **600**, 1771 (2006).

[101] A. F. Carley, S. D. Jackson, J. N. O'Shea, and M. W. Roberts, Surf. Sci. **440**, L868 (1999).

[102] M. W. Roberts and R. S. C. Smart, J. Chem. Soc. Faraday Trans. 1 Phys. Chem. Condens. Phases 2957 (1984).

[103] M. C. Biesinger, L. W. M. Lau, A. R. Gerson, and R. S. C. Smart, Phys. Chem. Chem. Phys. **14**, 2434 (2012).

[104] R. Eguchi, Y. Okamoto, Z. Hiroi, S. Shin, A. Chainani, Y. Tanaka, M. Matsunami, Y. Takata, Y. Nishino, K. Tamasaku, M. Yabashi, and T. Ishikawa, J. Appl. Phys. **105**, 56103 (2009).

[105] E. K. H. Salje, Phase Transitions **86**, 2 (2013).

[106] J. Chakhalian, J. W. Freeland, A. J. Millis, C. Panagopoulos, and J. M. Rondinelli, Rev. Mod. Phys. **86**, 1189 (2014).

[107] J. Matsuno, N. Ogawa, K. Yasuda, F. Kagawa, W. Koshibae, N. Nagaosa, Y. Tokura, and M. Kawasaki, Sci. Adv. **2**, e1600304 (2016).

[108] J. C. Agar, A. R. Damodaran, M. B. Okatan, J. Kacher, C. Gammer, R. K. Vasudevan, S. Pandya, R. V. K. Mangalam, G. A. Velarde, S. Jesse, N. Balke, A.

M. Minor, S. V. Kalinin, and L. W. Martin, Nat. Mater. **15**, 549 (2016).

[109] A. Aird and E. K. H. Salje, Eur. Phys. J. B **15**, 205 (2000).

[110] A. Aird and E. K. H. Salje, J. Phys. Condens. Matter **10**, L377 (1999).

[111] F. Arrouy, J.-P. Locquet, E. J. Williams, E. Mächler, R. Berger, C. Gerber, C. Monroux, J.-C. Grenier, and A. Wattiaux, Phys. Rev. B **54**, 7512 (1996).

[112] N. Sata, K. Eberman, K. Eberl, and J. Maier, Nature **408**, 946 (2000).

[113] J. Seidel, L. W. Martin, Q. He, Q. Zhan, Y.-H. Chu, A. Rother, M. E. Hawkridge, P. Maksymovych, P. Yu, M. Gajek, N. Balke, S. V Kalinin, S. Gemming, F. Wang, G. Catalan, J. F. Scott, N. A. Spaldin, J. Orenstein, and R. Ramesh, Nat. Mater. **8**, 229 (2009).

[114] L. Goncalves-Ferreira, S. A. T. Redfern, E. Artacho, and E. K. H. Salje, Phys. Rev. Lett. **101**, 97602 (2008).

[115] J. F. Ihlefeld, C. M. Folkman, S. H. Baek, G. L. Brennecka, M. C. George, J. F. Carroll, and C. B. Eom, Appl. Phys. Lett. **97**, 2010 (2010).

[116] S. Van Aert, S. Turner, R. Delville, D. Schryvers, G. Van Tendeloo, and E. K. H. Salje, Adv. Mater. **24**, 523 (2012).

[117] S. Kobayashi, Y. Ikuhara, and T. Yamamoto, Appl. Phys. Lett. **102**, 7 (2013).

[118] C. Sekar, T. Watanabe, and A. Matsuda, J. Cryst. Growth **212**, 142 (2000).

[119] C. Sekar, T. Watanabe, A. Matsuda, H. Shibata, Y. Zenitani, and J. Akimitsu, Int. J. Inorg. Mater. **3**, 1201 (2001).

[120] J. F. Bringley, B. A. Scott, S. J. La Placa, R. F. Boehme, T. M. Shaw, M. W. McElfresh, S. S. Trail, and D. E. Cox, Nature **347**, 263 (1990).

[121] J. F. Bringley, B. Scott, S. J. La Placa, T. McGuire, F. Mehran, M. W. McElfresh, and D. E. Cox, Phys. Rev. B **47**, 15269 (1993).

[122] A. Gupta, B. W. Hussey, A. M. Guloy, T. M. Shaw, R. F. Saraf, J. F. Bringley, and B. A. Scott, J. Solid State Chem. **108**, 202 (1994).

[123] Z. Hiroi and M. Takano, Nature **377**, 41 (1995).

[124] A. Webb, E. Skelton, S. Qadri, V. Browning, and E. Carpenter, Phys. Rev. B **45**, 2480 (1992).

[125] A. M. Abakumov, J. Hadermann, M. G. Rozova, B. P. Pavljuk, E. V Antipov, O. I. Lebedev, and G. van Tendeloo, J. Solid State Chem. **149**, 189 (2000).

[126] T. Endo, T. Kobayashi, T. Sato, and M. Shimada, J. Mater. Sci. **25**, 619 (1990).

[127] T. Katayama, A. Chikamatsu, H. Kamisaka, H. Kumigashira, and T. Hasegawa, Appl. Phys. Express **9**, 25801 (2016).

[128] T. Onozuka, A. Chikamatsu, T. Katayama, Y. Hirose, I. Harayama, D. Sekiba, E. Ikenaga, M. Minohara, H. Kumigashira, and T. Hasegawa, ACS Appl. Mater. Interfaces **9**, 10882 (2017).